

Article

Sodium Lauryl Sulfate-Conjugated Cationic Gemini-Surfactant-Capped Gold Nanoparticles as Model System for Biomolecule Recognition

Elia Grueso ^{1,*}, Rosa M. Giráldez-Pérez ^{2,*}, Rafael Prado-Gotor ¹ and Edyta Kuliszewska ³¹ Department of Physical Chemistry, University of Seville, 41012 Seville, Spain² Faculty of Science, Department of Cellular Biology, Physiology and Immunology, University of Córdoba, 14014 Córdoba, Spain³ Chemtra, 47-300 Krapkowice, Poland

* Correspondence: elia@us.es (E.G.); rgiraldez@uco.es (R.M.G.-P.)

† These authors contributed equally to this work.

Abstract: Surfactant-based nanostructures are promising materials for designing novel colorimetric biosensors based on aggregation/disaggregation phenomena. In this work, a colorimetric sensor based on the plasmonic shift of surfactant-capped gold nanoparticles via the disaggregation mechanism was developed. To perform this, the optimum SDS concentration was firstly determined in order to form Au@16-s-16/SDS complex aggregates with a well-defined SPR band in the blue region. Once the optimal SDS concentration for Au@16-s-16 aggregation was established, the sensing method depended on the nature of the electrostatic charge of the biopolymer studied where both the strength of the biopolymer/SDS and biopolymer/Au@16-s-16 interactions and the cationic gold nanoparticles play a key role in the disaggregation processes. As a result, an instantaneous color change from blue to red was gradually observed with increasing biopolymer concentrations. The response of the sensor was immediate, avoiding problems derived from time lapse, and highly dependent on the order of addition of the reagents, with a detection limit in the nanomolar and picomolar range for DNA and Lysozyme sensing, respectively. This behavior can be correlated with the formation of different highly stabilized Au@16-s-16/biopolymer/SDS complexes, in which the particular biopolymer conformation enhances the distance between Au@16-s-16 nanoparticles among the complexes.

Keywords: gold nanoparticles; gemini surfactants; colorimetric sensor; colloid aggregation–disaggregation; biopolymers



Citation: Grueso, E.; Giráldez-Pérez, R.M.; Prado-Gotor, R.; Kuliszewska, E. Sodium Lauryl Sulfate-Conjugated Cationic Gemini-Surfactant-Capped Gold Nanoparticles as Model System for Biomolecule Recognition.

Chemosensors **2023**, *11*, 207.

<https://doi.org/10.3390/chemosensors11040207>

Academic Editors: Iolanda Cruz Vieira, Edson Roberto Santana and João Paulo Winiarski

Received: 28 January 2023

Revised: 17 March 2023

Accepted: 22 March 2023

Published: 25 March 2023



Copyright: © 2023 by the authors. Licensee MDPI, Basel, Switzerland. This article is an open access article distributed under the terms and conditions of the Creative Commons Attribution (CC BY) license (<https://creativecommons.org/licenses/by/4.0/>).

1. Introduction

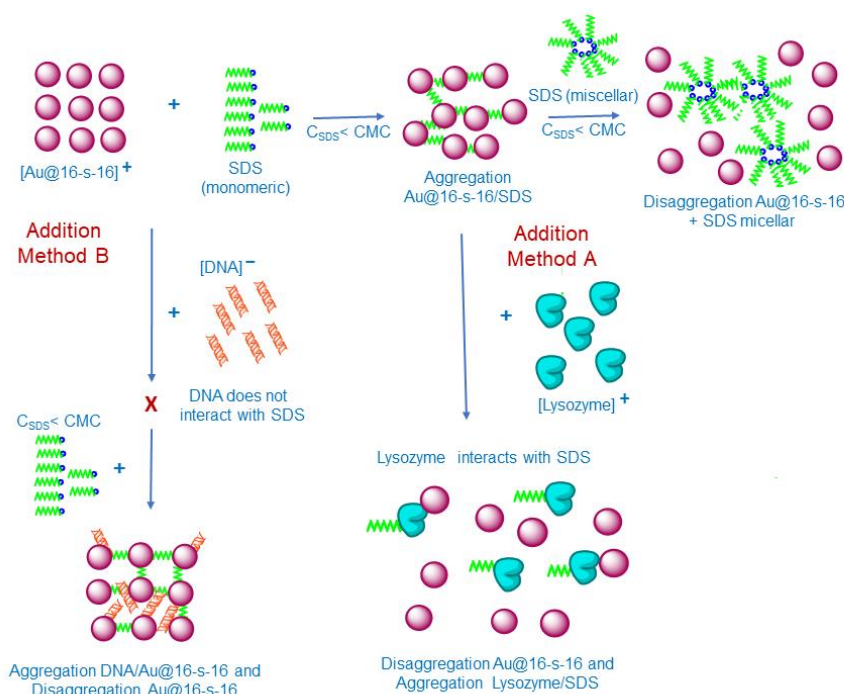
Accurate and reliable biopolymer determination is of immense importance not only for its role in the pharmaceutical industry but also for medical applications [1]. For instance, in the case of DNA, its successful detection can have an important impact on many important areas of research such as invasive-species research, medical diagnostics, drug development, or environmental health [2]. Additionally, DNA detection makes up an important tool in identifying the presence of genetic diseases such as cancer [3]. Likewise, protein detection has been shown to be useful for clinical diagnosis, treatment, and biological research [4]. In particular, Lysozyme is a cationic bacteriolytic protein and important biomarker whose abnormal concentration in serum and urine can be related to the presence of many diseases such as leukemia, meningitis, renal infection, and even the presence of cancer cells [5,6]. Importantly, in the case of lysozyme, the production of an excess of this protein, detectable in urine and other biological fluids such as blood serum, was shown to be a good indicator of the presence of monocytic and myelomonocytic leukemia (both subtypes of acute myeloid leukemia) in the 1960s [7,8]. Moreover, it was postulated that some alterations in

renal function are associated with these types of leukemia, which would cause a decrease in the reabsorption of lysozyme in the kidney, leading to a disease called lysozymuria [9]. Specifically, acute lymphoblastic leukemia, which is currently considered the main type of childhood leukemia, causes a sharp decrease in serum lysozyme concentration with respect to control cases [10,11]. In view of this great need, therefore, multiple biopolymer measurement methods have been developed such as colorimetry [12], Raman spectroscopy [13], fluorimetry [14], mass spectrometry [15], chromatography [16], gel electrophoresis [17], lab-on-chip methods [18], and electrochemical sensing [19]. For the conventional methods, such as DNA detection using fluorescent labels in combination with amplification by polymerase chain reaction (PCR), several major drawbacks still remain to be overcome. The main reason for this disadvantage is related to the need to use complex algorithms and expensive instrumentation [20]. Particularly in the case of the detection of proteins such as Lysozyme, in addition to the abovementioned limitations, high instrument dependence is combined with low sensitivity and time lapse due to the long period required for sample incubation [21]. Moreover, commercial kits for detecting serum Lysozyme concentration involve the use of expensive antibodies requiring preservation (limited to 2–8 °C) and qualified personnel to manipulate and analyze the samples [7,22]. Therefore, it is clear that further simplification in terms of the time, cost, instrumentation, and complexity of sample preparation is needed, with all of this needed to effectively take these implementations from the laboratory to the production line. Among these sensing modalities, colorimetric sensors based on nanoparticles (NPs) provide several great advantages in comparison with other sensing methods, such as the high capability of surface modification of nanoparticles and simple biorecognition [23]. Furthermore, since physicochemical properties including charge, hydrogen-bonding ability, hydrophobicity/hydrophilicity, and surface topology can easily be modulated on the surface of NPs, nanosystems provide a versatile scaffold for biosensor output [24]. Specifically, AuNPs can be readily fabricated in sizes comparable to proteins, facilitating high-affinity interactions [25]. In a recent work, anisotropic gold nanostructures were used in an electrochemical biosensor to detect cardiac troponin I, with a wide range of detection from 0.06 to 100 ng/mL with high selectivity [26]. In another work, a colorimetric sensor array based on walnut-like Au@MnO₂ nanoparticles and MnO₂ nanostars was developed for detecting alkaloids. The sensor is based on the etching of two kinds of nanomaterials by choline action [27]. The design and working principle of the colorimetric methods is based on significant changes in NPs' optical light absorption due to biopolymer recognition, and related changes in the position and intensity of the nanoparticles' SPR bands [23]. However, the major drawback of such colorimetric biosensors is related to the time needed for biopolymer recognition, since the mechanism of action of the majority of AuNPs-based colorimetric sensors is established in biopolymer-induced nanoparticle aggregation [28–33]. In fact, aggregation events are frequently time-dependent, with aggregation kinetics in the range of hours or even days, clearly limiting their practical application [34–40]. Our strategy relies on in situ reversible disaggregation processes induced by biopolymers starting from a previously aggregated colloidal system. Our initial biosensing studies involved biopolymer identification employing negatively charged Au@citrate nanoparticles linked to a monomeric cationic gemini surfactant, forming aggregated complexes as biopolymer receptors [41]. Our efforts have concurrently been directed towards enhancing the sensitivity of the method. For this reason, in this report, we used arrays of cationic gold nanoparticles covered with gemini surfactants featuring an SDS single-chain surfactant on the surface in order to obtain aggregated complexes.

The aim of this work was to develop a new method to detect large biomolecules with a well-defined global charge. To perform this, we selected DNA and Lysozyme as model systems of highly negative and positive charge biomolecules, respectively. The sensing strategy and detection mechanism of large biomolecules described in this work are illustrated in Scheme 1. At first, to carry out the biosensor construction, it was necessary to find out the SDS concentration at which gold colloid aggregation was maxima. When SDS concentrations are below the CMC, the SDS is in its monomer form and the favor-

able electrostatic and hydrophobic interactions among cationic Au@16-s-16 nanoparticles and the anionic surfactants induce the formation of Au@16-s-16/SDS aggregates. Then, for nanocomplex disaggregation processes induced by biomolecule addition, the global charge of them and their affinity for both SDS surfactant and cationic gold nanoparticles plays a key role, in such a way that when the biomolecules have a well-defined positive charge, as in the case of Lysozyme, a competitive binding for the SDS that forms part of the Au@16-s-16/SDS aggregates is given, promoting Au@16-s-16 disaggregation. Thus, sensor construction for positively charged biomolecules is based on the addition method, A, in which increasing concentrations of the positive biopolymer are added to the previously formed Au@16-s-16/SDS aggregates, promoting the gradual disaggregation of the complexes and a color change in the solution that passes from blue to red. Note that Au@16-s-16/Lysozyme/SDS complexes are also formed due to the high affinity of Au@16-s-16 nanoparticles with the biopolymer (see Scheme 1). On the other hand, when well-defined negative-charge biopolymers such as DNA are sensed, the interaction biopolymer/SDS is almost negligible and, thus, the competitive binding for the surfactant is not feasible. Thus, in this case, the addition method B is operative. In this way, the biopolymer is firstly added to the nanoparticles followed by the SDS surfactant at a fixed concentration that guarantees the maxima Au@16-s-16/SDS aggregation. As a result, the favorable interaction DNA/Au@16-s-16 causes gradual Au@16-s-16/SDS complex disaggregation with increasing biopolymer concentration. Consequently, the color of the solution gradually passes from blue to red. In the specific case of DNA, a well-defined Au@16-s-16/DNA/SDS network is formed in which gold nanoparticles are well separated from each other, guaranteeing the gold colloid disaggregation. Thus, the detection strategies involving Lysozyme and DNA are not the same and depend on the global charge of the biomolecule studied. Precisely, one of the advantages of this work compared with the previous one based on Au@citrate/12-s-12 complexes is the nature of the surfactant used to form the initial aggregates [41]. Note that the negative charge of SDS makes DNA/SDS interaction not feasible and, consequently, the method of detection changes depending on the global charge of the studied biopolymer. Moreover, two kinds of surfactants play a key role in the biosensor: (i) the positively charged 16-s-16 gemini surfactant that integrates the Au@16-s-16 nanoparticle and (ii) the negative charge SDS monomer. This results in the formation of more stable Au@16-s-16/SDS aggregates induced by the highly favored electrostatic and hydrophobic interactions among the surfactants. This characteristic of the new rearrangement allows a more gradual disaggregation process, expanding the range of concentrations in which the sensor response is linear as well as its sensitivity. On the other hand, another advantage of this work in comparison with the use of nanosystems based on surfactants is related to the simplicity of the sensor. In a previous work, an array of surfactant-stabilized gold nanoparticles that used CTAB or SDS as a monomeric surfactant was employed to distinguish different proteins. The results showed that higher protein concentrations in the solution were required to induce nanosystem aggregation under higher CTAB concentrations [42]. However, in this work, the sensor response is based on the use of fixed gold nanoparticle and SDS concentrations, which contributes to simplifying both the data analysis and sensor construction. Different methods based on colorimetric approaches and electrochemical methods have been developed to detect different biomolecules such as DNA or Lysozyme [43–46]. The main advantages of this work with respect to the previous ones are: (i) the rapid response of the sensor in the order of seconds which highly reduces the time cost for biomolecule determination, especially in the case of Lysozyme; (ii) the simplicity of the method that does not require qualified personnel for its determination and requires less complex protocols; (iii) the versatility of the method that permits detecting both positive- and negative-charge biomolecules by changing the addition order of the reactants; and (iv) the stability of the nanocomplexes which contributes to gaining reproducibility and storage stability for commercial purposes. Thus, the novel method is sensitive and fast compared with other colorimetric methods reported in the literature. For instance, a polymer–aptamer detection probe based on the AuNPs crosslinking strategy

has served to detect Lysozyme through the UV-visible technique with a detection limit of 4.4 nM [47]. In another recent work, this protein was detected in human urine based on the use of Au@citrate of 15 nm and colorimetric analysis based on CIEL*a*b* with a detection limit of 4 μ M [48]. In the case of DNA, Au@citrate nanoparticles were used to detect DNA based on SPR displacement with an LOD of 1 μ M [49]. In another work, a more complex nanosystem based on oligonucleotide-modified AuNPs was used to detect genomic DNA with an LOD of 600 pM [50]. The greater physicochemical interaction between Au@16-s-16/SDS and biopolymers permits their recognition from the molar to the nanomolar or picomolar range of concentration for DNA and Lysozyme, respectively, with Au@16-s-16 SPR band modification from blue to red at about 200 nm. Taken together, these studies demonstrate that through the tuning of the AuNPs receptor structure and charge, highly effective and sensitive array-based sensors for biopolymers can be produced. However, the mechanism of molecular recognition developed in this work should be individually designed and adapted taking into account the global charge of the biomolecule and the media used in the quantification to be able to expand the pool of available analytes.



Scheme 1. Proposed sensing strategy for biomolecule detection based on gold nanoparticle color changes.

2. Experimental Section

2.1. Materials

All commercial chemicals mentioned were of Anal. R. Grade. The biopolymers used were Lysozyme (from chicken egg white) and calf thymus DNA. Both reactants were purchased from Sigma-Aldrich-Merck KGaA (Darmstadt, Germany). Donor equine serum was purchased from Cultex (16SH30074.03, CULTEK, Hanover, Germany). Hydrogen tetrachloroaurate (III) trihydrate, sodium cacodylate, and 3-aminopropyltriethoxilane (APTES) were also purchased from Sigma-Aldrich-Merck KGaA (Darmstadt, Germany). Sodium borohydride (NaBH_4) was purchased from Panreac Química S.L.U (Barcelona, Spain). No protein contamination was evaluated measuring the absorbance ratio of DNA stock solutions at 260 nm and 280 nm ($A_{260}/A_{280} = 1.87$) [51]. The average number of DNA base pairs (mean bp) was tested in a previous work by using electrophoresis and ethidium bromide as biomarker. As a result, the DNA mean size in base pairs was higher than 10,000 [52]. DNA polynucleotide concentrations, given in phosphate groups, were determined spectrophotometrically from the molar absorptivity ($6600 \text{ M}^{-1} \text{ cm}^{-1}$ at 260 nm) [53].

The temperature of the samples was maintained at 298.0 ± 0.1 K in all the experiments, and the water used for preparing the samples had a conductivity of less than 10^{-6} Sm^{-1} . The working pH for the experiments in water and in horse serum media was 6.4 and 7.4, respectively. Total concentrations of DNA and Lysozyme biopolymers, gold nanoparticles covered with 16-s-16 gemini surfactant, and the SDS surfactant in a working solution will now be referred to as C_{DNA} , C_{Lysozyme} , $C_{\text{Au@16-s-16}}$ ($s = 3$ or 6), and C_{SDS} , respectively.

2.2. Synthesis and Characterization of Cationic 16-3-16 and 16-6-16 Gemini Surfactants

To synthesize the gemini surfactant compounds, 0.05 mol of α,ω -dibromoalkane and 0.12 mol of *N,N*-dimethylalkylamine was mixed in 100 mL of acetonitrile as the solvent. Then, the resulting solution was stirred under reflux for 20 h. Upon cooling, a white solid was recovered with filtration. The obtained samples were recrystallized from ethyl acetate. This process was repeated up to five times and, finally, the products were dried under a vacuum [54]. The gemini-obtained were characterized using the mass spectrometry technique [55], nuclear magnetic resonance spectroscopy, and elemental analysis. Critical micelle concentrations (CMC) of the surfactants were measured by using the surface tension technique. As a result, values of 2.4×10^{-5} M and 3.2×10^{-5} M for 16-3-16 and 16-6-16, respectively, were obtained at 298 K. The obtained results are in accordance with the values reported by Zana et al. [56]. For more details of gemini surfactant characterization, see the SI of this paper.

2.3. Synthesis of Au@16-3-16 and Au@16-6-16 Gemini-Surfactant-Capped Gold Nanoparticles

Gold nanoparticles functionalized with gemini surfactants were prepared following a similar process developed by our group [57]. A modification of the Turkevich method was used for which Au^{3+} ions were reduced to Au^0 ions using NaBH_4 as a reducing agent, obtaining stable nanoparticles [58]. Au@16-s-16 nanoparticles were synthesized using NaBH_4 (100 μL , 0.4 M) as a reductant for hydrogen tetrachloroaurate (III) hydrate ($\text{HAuCl}_4 \cdot 4\text{H}_2\text{O}$) (390 μL , 23 mM) and the appropriate gemini surfactant concentration as a stabilizing agent (30 mL of 16-3-16 or 16-6-16 gemini surfactant $1 \cdot 10^{-4}$ M aqueous solutions). A yellow solution that was stirred for 5 min was obtained at first when the surfactant was added to the gold. Then, a freshly prepared borohydride solution was added drop by drop to the gold–surfactant mixture. The sample was stirred moderately for 15 min in darkness and, finally, a reddish-color solution was obtained. TEM measurements and the ImageJ software program were used to characterize the size and morphology of the synthesized nanoparticles. For this, a sample set of over 200 nanoparticles was used. As a result, we obtained monodisperse Au@16-3-16 and Au@16-6-16 gold nanoparticles whose mean size was found to be 3.8 ± 0.8 nm and 4.1 ± 0.9 , respectively (see Figure S1). The total concentration of the colloidal stock solution was taken from the average nanoparticle size obtained from the TEM (see Section 2.4.3) and considering the reduction process was fully accomplished. As a result of this, $C_{\text{Au@16-s-16}}$ was 1.74×10^{-7} M and 1.38×10^{-7} M for Au@16-3-16 and Au@16-6-16, respectively.

2.4. Methods

2.4.1. UV/Vis Spectroscopy

A CARY 500 SCAN UV-vis-NIR (Ultraviolet/Visible/Near Infrared) UV-vis spectrophotometer (Varian, Markham, ON, Canada) was used to measure absorbance spectra, by using a standard quartz cell of 1 cm path length. The temperature of the measurements was fixed at 298.2 K and the wavelength range explored for measuring the spectra was 400–800 nm. The wavelength accuracy and spectral bandwidth were ± 0.3 and 1 nm, respectively. The Au@16-s-16/SDS samples prepared to study the aggregation process were incubated for 15 min to ensure the stabilization of the system after recording the absorbance spectra. In contrast, the disaggregation experiments of the complexes in the presence of biomolecules were carried out *in situ*. This is because we proved that the solutions were stabilized quickly. Absorbance titration experiments were carried out at a fixed colloidal

gold concentration of $C_{\text{Au@16-3-16}} = 1.74 \times 10^{-8}$ M and $C_{\text{Au@16-6-16}} = 1.38 \times 10^{-8}$ M for all the experiments. The samples were repeated three times and the relative error was calculated to be $< 5\%$. Moreover, it was checked that the samples were stable for at least 24 h of their preparation.

To measure biopolymer/16-s-16 equilibrium binding constants, a fixed $C_{16-s-16}$ was used, and $C_{\text{biopolymer}}$ varied from 5.0×10^{-8} M to 8.0×10^{-4} M and from 5.0×10^{-9} M to 1.0×10^{-4} M for DNA and lysozyme, respectively. Absorbance data at 525 nm and 516 nm were then analyzed in accordance with the Hildebrand–Benesi model for Au@16-3-16/biopolymer- and Au@16-6-16/biopolymer-based systems, respectively [59,60] (see Section 3.2 for more details).

2.4.2. Deconvolution Procedure

The deconvolution of experimental absorbance spectra was carried out with the help of Fityk deconvolution software (version 0.9) [61]. The absorbance spectra of distinct nanosystems were always fitted to two Gaussian functions. The deconvolution model was based in the use of two absorbance bands: one of them centered at around 526–548 nm and 515–551 nm for Au@16-3-16/SDS and Au@16-6-16/SDS systems, respectively, that was assigned to the nonaggregated nanoparticles, and another Au@16-s-16 absorbance band quite far above 540 nm that was associated with aggregated nanoparticles. The second band can be assigned to particles with different size distributions depending on the aggregation state of the analyzed sample. Moreover, a variable linear function was included to ensure the best fit. The functionality of the added function was to correct the possible effect of residual gold salts remaining in the solution as well as the effect of light scattering phenomena in each sample [62,63].

2.4.3. TEM Measurements

Isolated gemini surfactant nanoparticles and Au@16-s-16/SDS complexes were placed on a copper grid coated with a carbon film for TEM examinations. The samples were dispersed in water as solvent and a total of 10 μL of nanoparticles or the complex solution was dropped onto the copper grid. The samples were then air-dried at room temperature for a period of 2 h. The size of gold nanoparticles was analyzed in Figure S1. EDS measurements were employed to confirm the presence of gold in the Au@16-s-16/SDS complexes. Figure S2 shows EDS spectra in which the presence of K and L lines associated with the gold element demonstrated the presence of gold in the nanocomplex. Moreover, the intensity (counts) versus position (nm) profiles for Au@16-s-16/SDS complexes provided values of $d = 0.24$ nm in both nanosystems (see Figure S3). TEM analysis was performed in a high-resolution TEM-TALOS F200S electron microscope (FEI Company, Hillsboro, OR, USA) equipped with an energy-dispersive X-ray spectrometer and working at 200 kV. ImageJ 1.52a software was used to analyze the obtained TEM images.

2.4.4. Zeta Potential Measurements

The zeta potential charges of the free nanoparticles and Au@16-s-16/SDS complexes were measured in water after 15 min of sample preparation and stabilization. A Zetasizer Nano ZS from Malvern Instrument Ltd. (Worcestershire, UK), which employs a laser Doppler velocimeter (LDV) to quantify the velocity of the particles based on their electrophoretic mobility, was used to measure the Zeta potential (ζ) values. The type of cell used was a DTS1060 polycarbonate capillary cell thermostated to 298 K. The number of sample repetitions was at least six in each case. To prepare the samples, $C_{\text{Au@16-s-16}}$ concentrations were fixed at 1.74×10^{-7} M and 1.38×10^{-7} M for Au@16-3-16 and Au@16-6-16, respectively, while C_{SDS} was varied from 1.0×10^{-6} M to 1.0×10^{-3} M.

2.4.5. Atomic Force Microscopy Measurements (AFM)

The AFM micrographs were obtained with a Molecular Imaging Picoscan 2500 (Agilent Technologies, Las Rozas, Madrid, Spain). Images were registered in air and in tapping

mode using scan speeds of 0.5 Hz. To perform this, silicon cantilevers (Model Pointprobe, Nanoworld Neuchâtel, Switzerland) were used; the resonance frequency was 240 kHz and the nominal force constant was 42 N/m. In order to guarantee the correct complex formation, in all cases, the total biopolymer concentrations were fixed at 5.0×10^{-5} M and 1.0×10^{-5} M for DNA and Lysozyme, respectively. These concentrations were selected in accordance with results obtained from TEM microscopy and UV-visible spectrophotometric titrations. To prepare samples for AFM visualization, a freshly cleaved mica surface was firstly modified with 0.1% (*v/v*) APTES in water solution. An incubation time of 20 min was used to modify the mica surface with APTES. This process was followed by washing of the surface with ultrapure water, which was then dried with air. Next, a total of 100 μ L of each sample was dropped onto the APTES-modified mica surface. After 60 min of adsorption, the sample was washed with doubly distilled water and then air-dried. Subsequently, the AFM images were acquired and flattened to remove the background slope [64].

3. Results and Discussion

3.1. Au@16-*s*-16 Aggregation Induced by Anionic SDS Surfactant: Optimization of Biosensor Configuration

As previously mentioned, contrary to what occurs in aggregation processes, disaggregation processes occur instantaneously under the appropriate conditions. Consequently, for the development of an efficient response in a biosensor, it could be relevant to find a system configuration permitting the study of colloidal gold disaggregation phenomena. Thus, the first step of this work was to determine the optimum SDS concentration to induce Au@16-*s*-16 aggregation in the absence of any added biomolecule. For this purpose, it is crucial to find a well-defined SPR band of the Au@16-*s*-16/SDS aggregated complex located in the blue region around 600–700 nm. Firstly, it allows the incorporation of an SDS anionic surfactant to cationic Au@16-*s*-16 gold nanoparticles, and the formation of the complex is fundamentally promoted by attractive electrostatic interaction. At concentrations below the CMC of the anionic surfactant [65], SDS monomer interactions promote gold nanoparticle aggregation, leading to a color change in the solution from red to blue, visible to the naked eye (see Figures S4 and S5). Moreover, when we represent the maximum wavelength of the SPR band for the aggregation of the Au@16-*s*-16/SDS systems as a function of C_{SDS} concentration, it is possible to distinguish the optimum aggregation of Au@16-*s*-16 nanoparticles in the maximum observed for Figures S4 and S5, that is, 651 nm and 650 nm for Au@16-3-16/SDS and Au@16-6-16/SDS systems, respectively, at a C_{SDS} concentration of 30 μ M in both cases. In addition, Figures 1A and S6A denote a great shift in the maximum wavelength of the SPR band of 125 nm and 135 nm for Au@16-13-16 and Au@16-6-16, respectively, where the maximum passes from 526 nm (in the absence of SDS) to 651 nm for Au@16-13-16, and from 515 nm to 650 nm in the case of the analogous *s* = 6 derivative. As previously mentioned, this behavior can be explained considering the favorable electrostatic interaction between the anionic SDS surfactant and the positively charged Au@16-*s*-16 nanoparticle. It is important to note that the positive charge of the particles emerges from the adsorption of the 16-*s*-16 cationic gemini surfactants onto the colloid's surface. Note that this process occurs when gold nanoparticles are synthesized [57]. It is significant that the aggregation process is progressive and time-dependent as to when a purple color is observed (see Figures S4 and S5) and a time lapse of approximately 15 min is required for Au@16-*s*-16/SDS complex stabilization working below the CMC. Furthermore, when we analyzed the absorbance results in depth, we noted that changes in the maximum SPR bands for both systems upon aggregation were accompanied by a shift in the absorbance intensities at the maximum wavelength (650 nm and 651 nm for *s* = 3 and *s* = 6 nanosystems, respectively) to higher values (see Figures 1C and S6C), together with a concurrent decrease in the absorbance intensities at 526 nm and 515 nm for the *s* = 3 and *s* = 6 systems, respectively, whose wavelengths were selected to represent the behavior of the nonaggregated systems. However, starting from $C_{\text{SDS}} = 30 \mu\text{M}$ above the maximum aggregation concentration, the trend in the absorbance spectra with C_{SDS}

concentrations was opposite to that previously described (see Figures 1B and S6B). In this sense, the absorbance intensity clearly decreased at the maximum wavelength (in blue) and increased at the minimum wavelength (in red). Therefore, two zones can be clearly distinguished in the graph of the absorbance data versus C_{SDS} concentrations: a change zone and a stabilization zone that begin near the CMC value (see Figures 1D and S6D). Furthermore, the final state of the system at the higher SDS concentration was similar to the Au@16-s-16 isolated system; namely, when the surfactant self-assembled into micelles over CMC, no color change was observed with respect to the control. According to the bibliography, a valid explanation for this behavior would be that the formation of SDS micelles allows the Au@16-s-16 nanoparticles to remain separated from each other through steric impediment even upon interaction with the surfactant [66,67].

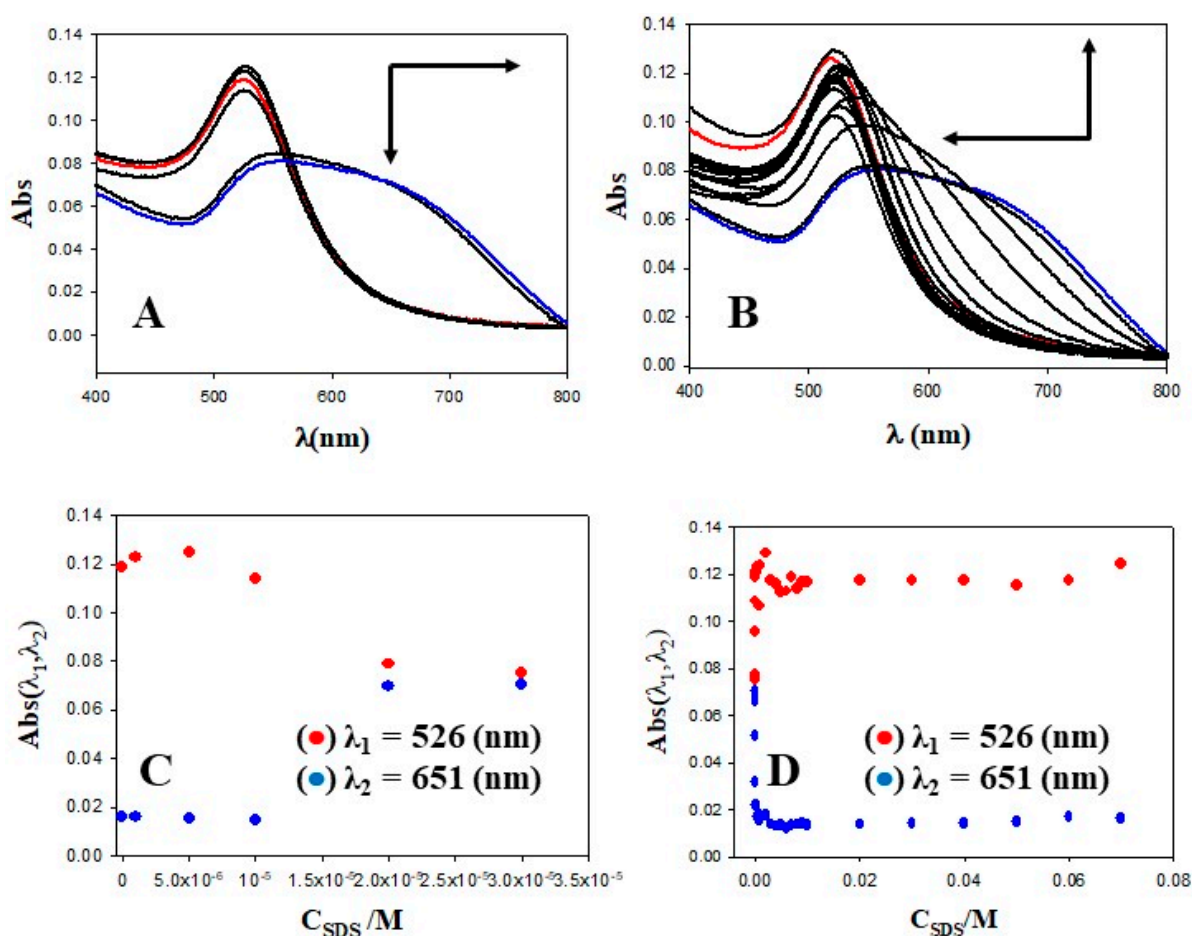


Figure 1. Absorbance titration of the Au@16-3-16/SDS system at a fixed $C_{\text{Au@16-s-16}} = 1.74 \times 10^{-8} \text{ M}$ concentration and its corresponding absorbance intensities at $\lambda_1 = 526 \text{ nm}$ and $\lambda_2 = 651 \text{ nm}$ wavelengths. (A) Aggregation experiments. Red spectrum, $C_{\text{SDS}} = 0 \mu\text{M}$; blue spectrum, $C_{\text{SDS}} = 30.0 \mu\text{M}$; black-spectrum arrow direction, $C_{\text{SDS}} = 1.0, 5.0, 10.0$ and $20.0 \mu\text{M}$. (B) Disaggregation experiments. Red spectrum, $C_{\text{SDS}} = 0.07 \text{ M}$; blue spectrum, $C_{\text{SDS}} = 30.0 \mu\text{M}$; black-spectrum arrow direction, $C_{\text{SDS}} = 40.0 \mu\text{M}, 50.0 \mu\text{M}, 60.0 \mu\text{M}, 75.0 \mu\text{M}, 10.0 \text{ mM}, 50.0 \text{ mM}, 75.0 \text{ mM}, 1.0 \text{ mM}, 2.0 \text{ mM}, 3.0 \text{ mM}, 4.0 \text{ mM}, 5.0 \text{ mM}, 6.0 \text{ mM}, 7.0 \text{ mM}, 8.0 \text{ mM}, 9.0 \text{ mM}, 0.01 \text{ M}, 0.02 \text{ M}, 0.03 \text{ M}, 0.04 \text{ M}, 0.05 \text{ M},$ and 0.06 M . (C) Absorbance intensities of aggregation experiments versus C_{SDS} . (D) Absorbance intensities of disaggregation experiments versus C_{SDS} .

However, this model of interaction is highly conditioned by the nanoparticle/micelle size ratio. In our case, the mean diameter of the Au@16-s-16 nanoparticles was found to be 3.8 nm and 4.1 nm for the $s = 3$ and $s = 6$ derivative, respectively. Furthermore, the published values for the diameter of an SDS anionic micelle are between 3.5 and 4.0 nm,

very similar to gold nanoparticles in solution [68,69]. Accordingly, it is reasonable to assume that for C_{SDS} concentrations over CMC, the interaction of the negatively charged micelles with positively charged gold nanoparticle surfaces acts as a steric impediment among nanoparticles, avoiding colloidal aggregation. Additionally, at concentrations below but close to CMC, the formation of surfactant aggregates on Au@16-s-16 nanoparticles could be the reason for the observed gradual color change, becoming purple in solutions near CMC. In light of this, since the formation of the micelles is not yet fully completed, it seems that the size of the aggregates can in part prevent the aggregation phenomena (see Figures S4 and S5). At concentrations over CMC, the surfactant–gold solutions returned to the red color exhibited by isolated nanoparticles, and no aggregation was observed. Note that these results are in good agreement with the model proposed by Kazakova et al., who studied the interactions of citrate-capped gold nanoparticles with an SDS surfactant [67].

The color changes observed, and thus the associated changes in the maximum wavelength of Au@16-s-16/SDS systems, can be used to give an approximation of the CMC of SDS surfactants. Therefore, a graphical representation of the SPR maximum wavelength (λ_{MAX}) with C_{SDS} near and above CMC allowed us to distinguish two very distinct branches that can be assimilated in two straight lines (see Figure 2). CMC was then calculated through the intersection of those lines. The implementation of this methodology for CMC determination through λ_{MAX} measurements gave very close values for SDS by using both Au@16-s-16 systems: a value of 7.2×10^{-3} M and 7.7×10^{-3} M for $s = 3$ and $s = 6$ derivatives, respectively. Note that these CMC values in water are in good agreement with those reported by Khan et al. [70] who found a CMC value of 8.0×10^{-3} M.

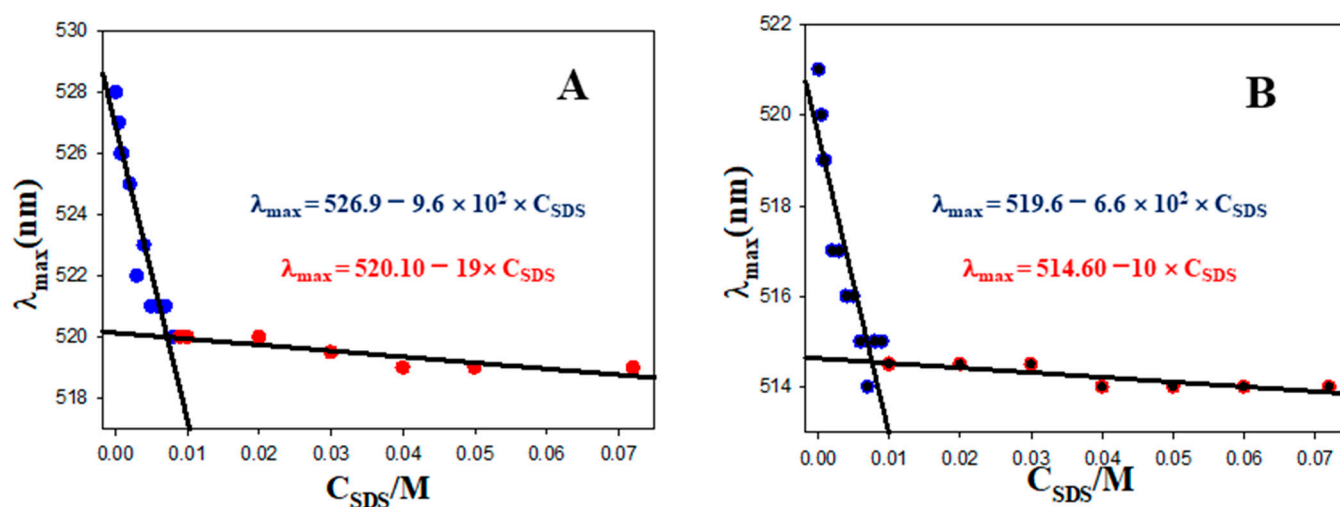


Figure 2. CMC determination for SDS surfactant following changes in maximum SPR wavelength. (A) Au@16-3-16/SDS system. (B) Au@16-6-16/SDS system.

It is important to note that a better approximation was obtained for CMC determination employing Au@16-s-16 λ_{MAX} measurements than that based on the use of Au@citrate of 10 nm core size, where a CMC value of 7.5×10^{-4} M in the presence of 0.01 M of NaCl was found [67], in comparison with data previously reported by Williams et al. of 1.46×10^{-3} M under identical experimental conditions [71]. This fact can be explained taking into account two fundamental differences with previous similar methodology: the smaller diameter of Au@16-s-16 nanoparticles compared to Au@citrate and the cationic character of the gemini-surfactant-based nanosystem. Therefore, one of the applications of this colorimetric system based on cationic gold nanoparticles is the CMC determination of distinct anionic surfactants. Finally, the SPR experimental spectra of Au@16-s-16/SDS systems were analyzed in depth using a simple deconvolution procedure in order to obtain the isolated contribution of each individual band. For this purpose, the experimental spectra were divided into two contributions: the band corresponding to the nonaggregated

and the aggregated system with $\lambda_{1,\max}$ and $\lambda_{2,\max}$ as characteristic parameters, respectively, as well as its corresponding area of peaks (see Section 2.4.2). The data in Table 1 show that the nonaggregated system is represented by a narrow peak, $\lambda_{1,\max}$, which varies between 526 and 548 nm and 515 and 551 nm for Au@16-3-16/SDS and Au@16-6-16/SDS systems, respectively. Consequently, this peak corresponds not only to the isolated gold nanoparticle but also to the nonaggregated complexes formed between Au@16-s-16 and SDS in monomeric and micelle forms.

Table 1. Deconvolution parameters for the experimental spectra obtained by Au@16-3-16/SDS and Au@16-6-16/SDS systems.

Au@16-3-16/SDS System			Au@16-6-16/SDS System		
$C_{\text{SDS}}(\text{M})$	$\lambda_{1,\max}/\text{nm}$ (Area ₁)	$\lambda_{2,\max}/\text{nm}$ (Area ₂)	C_{SDS}/M	$\lambda_{1,\max}/\text{nm}$ (Area ₁)	$\lambda_{2,\max}/\text{nm}$ (Area ₂)
0	526	—	0	515	—
1.0×10^{-6}	527	—	1.0×10^{-6}	517	—
5.0×10^{-6}	528	—	5.0×10^{-6}	518	—
1.0×10^{-5}	528	—	1.0×10^{-5}	519	—
2.0×10^{-5}	547 (2.03)	646 (9.02)	2.0×10^{-5}	550 (1.83)	648 (10.81)
3.0×10^{-5}	548 (1.94)	651 (10.17)	3.0×10^{-5}	551 (1.82)	650 (10.84)
4.0×10^{-5}	547 (2.03)	647 (9.01)	4.0×10^{-5}	534 (3.39)	605 (6.39)
5.0×10^{-5}	540 (2.28)	615 (7.06)	5.0×10^{-5}	524 (1.12)	571 (5.09)
6.0×10^{-5}	533 (2.51)	589 (5.56)	6.0×10^{-5}	524 (1.08)	569 (5.21)
7.5×10^{-5} (*)	531	—	7.5×10^{-5}	528	—

(*) Data specification for the first concentration at which the deconvolution process is not necessary for each system.

In addition, the broader red-shifted peak, $\lambda_{2,\max}$, was only due to the assembly of Au@16-s-16 in the presence of monomeric SDS, since from $C_{\text{SDS}} = 75 \mu\text{M}$, only a single peak was visualized and the deconvolution procedure was not needed. On the basis of the results given in Table 1, the magnitude of the aggregation–disaggregation processes measured using the maximum changes registered in both peaks was very similar in both Au@16-s-16 systems. However, these processes were only slightly greater in the case of Au@16-6-16, which is in accordance with the more precise CMC value obtained for this system. To verify or not the aggregation/disaggregation processes of gold nanoparticles detected with the absorbance spectroscopy technique as a consequence of anionic SDS surfactant addition, TEM experiments were carried out (see Figure 3).

To verify the aggregation/disaggregation processes of gold nanoparticles detected with the absorbance spectroscopy technique as a consequence of anionic SDS surfactant addition, TEM and DLS experiments were carried out. Two different aggregation states for the Au@16-s-16/SDS systems can be observed as a function of the SDS concentration. When the SDS concentration was far below the value of the CMC of SDS in water, large-size aggregates could be seen (see Figure 3A–F). Hence, the interaction of monomeric anionic SDS surfactant with highly cationic gold nanoparticles covered with 16-3-16 and 16-6-16 gemini surfactant resulted in colloid aggregation, where favorable electrostatic and hydrophobic interactions probably played a key role in this process. Note that the size of the aggregates was very similar in the two nanosystems explored, with values that varied between 200 and 800 nm, revealing that the nature of the spacer length was negligible. However, for solutions prepared at SDS concentrations very near or above the CMC, the disaggregation process took place in both Au@16-s-16/SDS systems (see Figure 3G–I). A close examination of Figure 3I reveals that SDS micelles could probably act as an electrostatic barrier for Au@16-s-16 aggregation, showing well-spaced colloids. Note that this assumption is in accordance with the model proposed by Kazakova et al. and Kuong et al. [66,67] in that when the surfactant concentration was above CMC, the formation of the micelles led to the separation of distinct nanoparticles and the solution turned red. In addition, as the nanoparticle/SDS micelle size ratio was close to 1 in both cases (1.01 for $s = 3$ and 1.09

for $s = 6$ derivative), steric hindrance between the nanoparticles and SDS micelles could reinforce the disaggregation phenomena. Both aggregation/disaggregation behaviors described using the TEM measurement were in good agreement with the results obtained using DLS and spectrophotometric titration, showing a corresponding increase/decrease in both the hydrodynamic size of the complexes and the spectra maximum wavelength with varying SDS concentrations. The results obtained from DLS are given in Table 2 and Figure S7, showing different steps of aggregation/disaggregation processes observed for Au@16-s-16/SDS nanosystems.

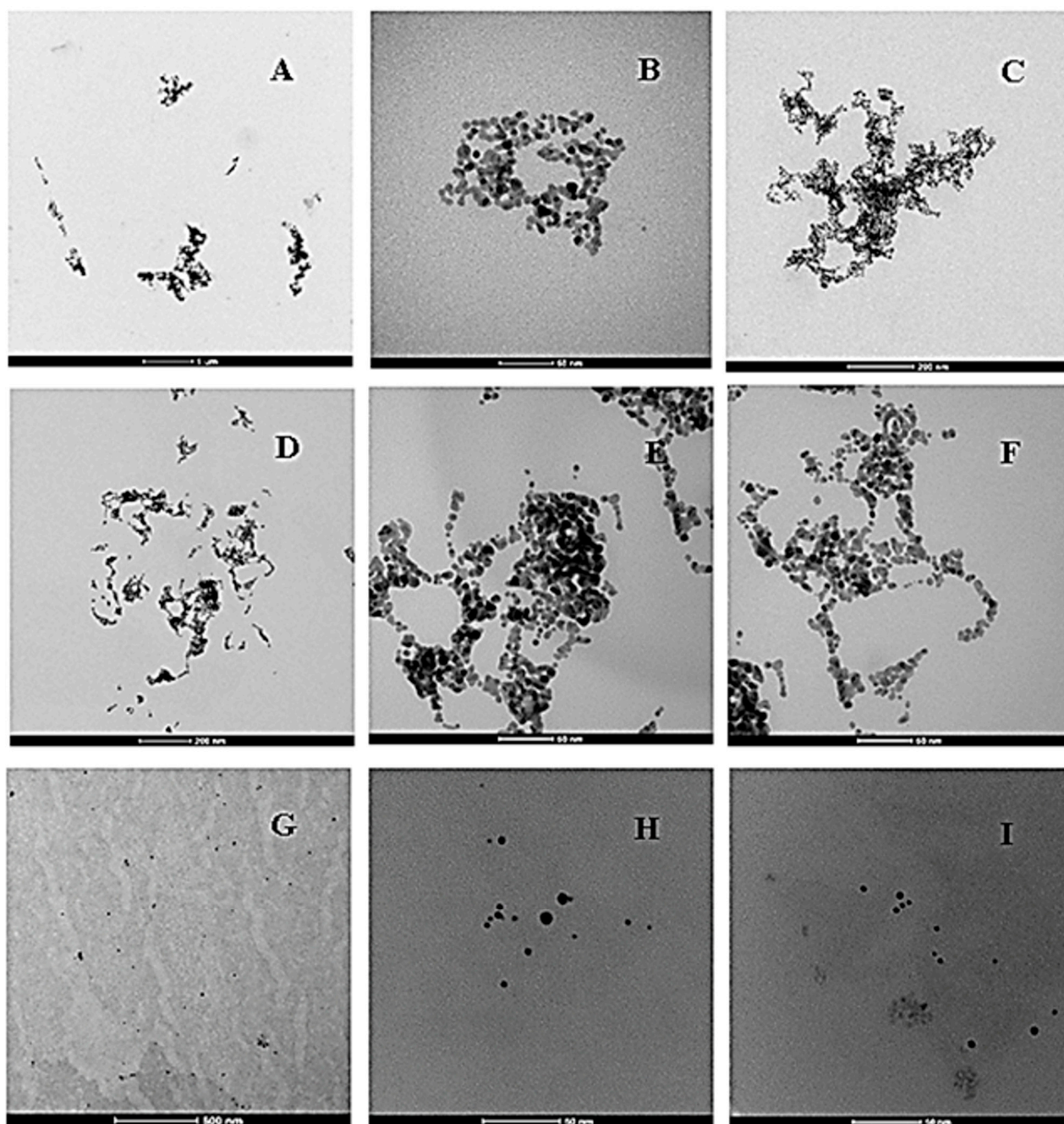
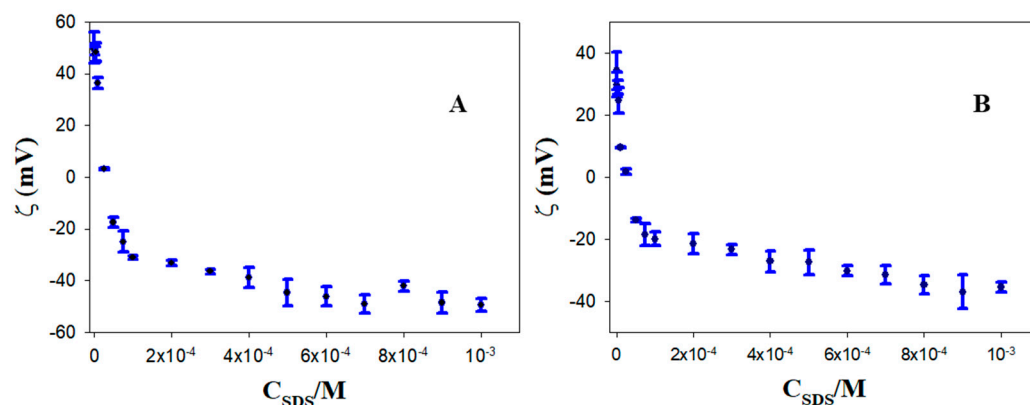


Figure 3. TEM images of aggregation/disaggregation processes for Au@16-s-16 nanoparticles in the presence of monomers and micelles of SDS, $C_{\text{Au@16-3-16}} = 1.74 \times 10^{-8}$ M and $C_{\text{Au@16-6-16}} = 1.38 \times 10^{-8}$ M in the samples. (A–C) Au@16-3-16/SDS system, $C_{\text{SDS}} = 3.0 \times 10^{-5}$ M; (D–F) Au@16-6-16/SDS system, $C_{\text{SDS}} = 3.0 \times 10^{-5}$ M; (G,H) Au@16-3-16/SDS system, $C_{\text{SDS}} = 1.5 \times 10^{-3}$ M; (I) Au@16-6-16/SDS system, $C_{\text{SDS}} = 1.5 \times 10^{-3}$ M.

Table 2. Values of the hydrodynamic diameters of different Au@16-s-16 nanoparticles and Au@16-s-16/SDS structures.

C_{SDS}/M	Au@16-3-16/SDS	Au@16-6-16/SDS
0	(3.6 ± 0.5) nm	(3.9 ± 0.5) nm
5.0×10^{-5}	(748 ± 11) nm	(400 ± 12) nm
1.0×10^{-3}	(18 ± 4) nm	(15 ± 4) nm

Considering the hydrodynamic sizes values in Table 2, it can be concluded that at C_{SDS} below the CMC, the diameters of the Au@16-3-16/SDS aggregates was greater than those of the analogous Au@16-6-16/SDS nanosystem. Furthermore, at C_{SDS} above the CMC, the size of the Au@16-s-16 structures was not exactly the same as that observed in the absence of the monomeric surfactant. This result seems to support the idea that SDS micelles play a key role in Au@16-s-16 disaggregation in the absence of biomolecules (see Scheme 1). Despite the fact that the aggregation/disaggregation processes have been verified using absorbance spectroscopy, DLS and TEM microscopy techniques, the possibility that electrostatic forces may mediate such SDS/Au@16-s-16 interactions still needs to be confirmed. In order to verify the importance of electrostatic Au@16-s-16/SDS interactions, zeta potential experiments were performed; the results are given in Figure 4.

**Figure 4.** Zeta potential of the gold nanoparticles as a function of the SDS concentrations. (A) Au@16-3-16/SDS system. (B) Au@16-6-16/SDS system.

As shown in Figure 4A,B, for both systems, the highly positive charge of the free gold nanoparticle strongly diminished when a small quantity of SDS surfactant was added to the solution, in such a way that the charge switched from 50 mV to 3.1 mV and from 34.3 mV to 1.7 mV at 2.5×10^{-5} M for the Au@16-3-16/SDS and Au@16-6-16/SDS systems, respectively. The charge was then inverted to a small global negative charge of -17.5 mV and -14 mV at 5.0×10^{-5} M, and remained below -20 mV up to 6.5×10^{-5} M. Note also that these results are in good agreement with the data in Table 1, in which the deconvolution of the measured spectra was needed for both systems from 2.0×10^{-5} M to 6.0×10^{-5} M due to the overlapping spectra of the free and aggregated colloid in the solution. As is known, low values of zeta potential may be associated with colloid aggregation/flocculation phenomena that occur due to the action of van der Waals attractive forces among the nanoparticles [72]. Hence, it is clear from the zeta potential analysis that the driving forces for particle aggregation are mainly electrostatic in nature. Moreover, the observed sharp decrease in zeta potential at C_{SDS} values below the CMC is in accordance with the idea that the coating of SDS is responsible for the Au@16-s-16 aggregation at concentrations well below the CMC. This fact contributes to the destabilization of the colloidal suspension by eliminating nanoparticle repulsions.

Once the changes in the nanoparticle aggregation state as a function of C_{SDS} concentrations were analyzed in depth using UV-vis, TEM, DLS and zeta potential techniques, the

optimization of the biosensor configuration was tackled. The sensor was prepared in two consecutive steps: (i) the formation of aggregated Au@16-s-16/SDS complexes as a starting point, followed by (ii) the disaggregation phenomena of the formed complexes, induced by the nanoparticle/biopolymer interaction which occurred gradually as a function of $C_{\text{biopolymer}}$. As previously discussed, at concentrations below the CMC for SDS, the direct interaction between the monomeric anionic surfactant and the gold nanoparticle induced the aggregation of the system, leading to a color change from red to blue easily detected by the naked eye. Thus, taking into account the C_{SDS} concentration needed for the maximum colloid aggregation ($C_{\text{SDS}} = 30 \mu\text{M}$), the formation of Au@16-s-16/SDS complexes was firstly accomplished. To this end, a mixture of gold nanoparticles and SDS with final concentrations of $C_{\text{SDS}} = 30 \mu\text{M}$ and nanoparticle concentrations of $C_{\text{Au@16-3-16}} = 1.74 \times 10^{-8} \text{ M}$ or $C_{\text{Au@16-6-16}} = 1.38 \times 10^{-8} \text{ M}$, respectively, was first prepared, giving blue colloidal solutions. The colloid disaggregation phenomenon was then induced by adding increasing amounts of biopolymer to the aggregated Au@16-s-16/SDS complexes, with the changes in the aggregation state of the nanosystem being mediated by the strong interaction between the biopolymer and gold nanoparticles. As a result, the color of the solution gradually changed from blue to red. These changes were accompanied by quantitative changes in the maximum SPR band as a function of $C_{\text{biopolymer}}$, leading to biopolymer sample quantification. The method suitability was tested using DNA and Lysozyme as examples of model systems for biomolecule recognition, working in a concentration range from 1.0 nM to 0.55 mM and from 1.0 pM to 0.1 mM for DNA and Lysozyme biopolymers, respectively. Two possible addition orders were analyzed for each nanosystem. In method A, the surfactant was first added to the nanoparticle solution, followed by the biopolymer. In method B, the addition order was the opposite:

(A) Au@16-s-16 + SDS + Biopolymer;

(B) Au@16-s-16 + Biopolymer + SDS.

As a result, no significant changes in the color or SPR band position were obtained for DNA detection in method A or lysozyme detection in method B, independent of the biopolymer concentration. Moreover, the gold nanosystem underwent aggregation features in all samples. Therefore, we considered discarding these methods in the explored nanosystems. However, considerable changes were registered for the opposite method in each system, namely for method B for DNA and method A for Lysozyme. The spectrophotometric results are given in Figures 5,6 and S8.

From these results, it can be deduced that DNA can protect gold nanoparticles against the SDS aggregation, with this protective effect being greater with increasing $C_{\text{biopolymer}}$. These results are in line with those for the interaction of Au@citrate nanoparticles with DNA in the presence of low NaCl electrolyte concentrations, in which such favorable DNA/Au@citrate interactions protect the nanosystem from salt-induced aggregation [57].

However, the most striking feature of this work is the way in which Lysozyme was able to induce Au@16-s-16/SDS disaggregation following addition method A, where Au@16-s-16 and SDS were previously mixed together. This effect could be due to two possible causes: (i) the interaction between the Lysozyme and SDS, with SDS sequestration in the biopolymer structure hindering the aggregation of the nanosystem, or (ii) the direct Lysozyme/Au@16-s-16 interaction that induces SDS liberation to the bulk solution, including the possibility of induced biopolymer conformational changes. To analyze these possibilities in depth and shed light on the sensing mechanism for DNA and Lysozyme, in the next section, we evaluate both the binding interactions between the species and the structural features of these interactions.

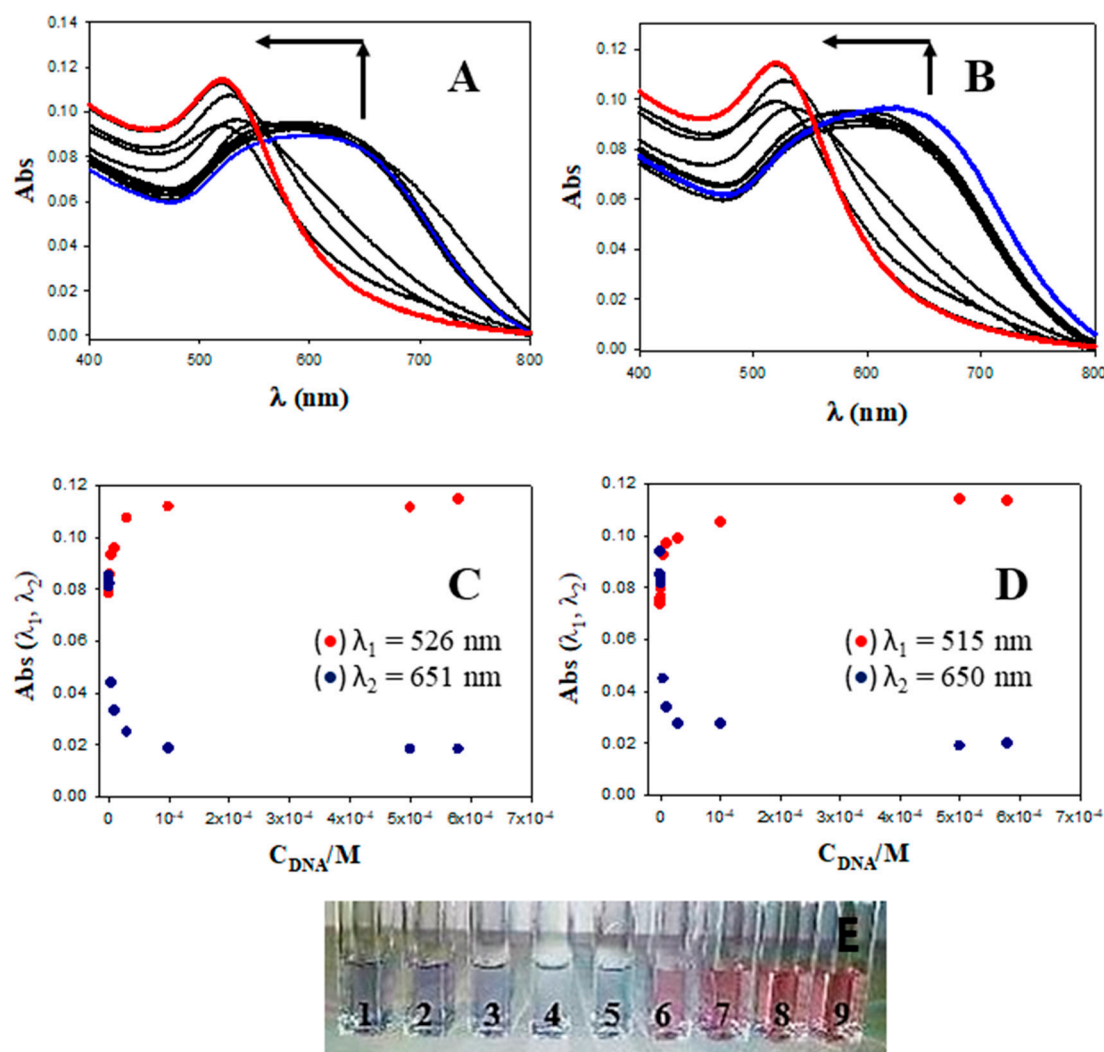


Figure 5. Absorbance titration of aggregated Au@16-s-16/SDS nanosystems at different C_{DNA} concentrations (addition method B). (**A,B**) $C_{DNA} = 0 \mu\text{M}$ (blue spectrum), $C_{DNA} = 580 \mu\text{M}$ (red spectrum), $C_{DNA} = 0.050, 0.10, 0.50, 0.75, 1.00, 5.00, 10.0, 30.0, 100.0,$ and $500.0 \mu\text{M}$ (black spectrum, arrow direction). (**C,D**) Absorbance versus C_{DNA} , red (nonaggregated nanoparticles) and blue points (aggregated nanoparticles) correspond to absorbance data at fixed wavelength. (**A,C**) Au@16-3-16/SDS/DNA system and (**B,D**) Au@16-6-16/SDS/DNA system. (**E**) Detailed view of corresponding color changes for Au@16-3-16/SDS/DNA system. (1) $C_{DNA} = 0 \mu\text{M}$, (2) $C_{DNA} = 0.050$, (3) $C_{DNA} = 0.10$, (4) $C_{DNA} = 0.50$, (5) $C_{DNA} = 1.0 \mu\text{M}$, (6) $C_{DNA} = 10.0 \mu\text{M}$, (7) $C_{DNA} = 30.0 \mu\text{M}$, (8) $C_{DNA} = 100.0 \mu\text{M}$, and (9) $C_{DNA} = 580.0 \mu\text{M}$.

3.2. Binding Interactions and Sensing Mechanism for DNA and Lysozyme Detection

The anionic surfactant SDS interacts with cationic Au@16-s-16 gold nanoparticles but not with DNA [73]. Thus, to avoid SDS-induced nanoparticle aggregation, it is necessary to add the biopolymer to the mixture before adding the anionic surfactant. Hence, optimal colorimetric changes were obtained with addition method B. In contrast to this, in the case of Lysozyme, the situation is completely different: SDS forms a stable complex with lysozyme without causing gross conformational changes in the enzyme molecule [74]. The great strength of the binding is controlled by both the hydrophobic regions and positive charges of the protein, and the hydrophobic tail and the negative charge of the detergent, with an association constant of $514 \text{ (M}^{-1}\text{)}$ in direct SDS micelles [75,76]. The binding enthalpy determined from the ITC isotherm depends on the SDS concentration: at a low SDS concentration ($<3 \text{ mM}$), it was -7.15 kJ/mol , indicating that binding was

predominantly via the electrostatic interaction, while at high surfactant concentrations, the nature of binding was cooperative, with the equilibrium binding constant decreasing exponentially with increasing lysozyme concentration [77]. Thus, since Lysozyme is able to interact with SDS, a competitive binding between SDS and Lysozyme for gold nanoparticles could be responsible for the optimal colorimetric changes registered with addition method A. The equilibrium binding constants for biopolymer/Au@16-s-16 can be determined following the absorbance changes at the maximum SPR for Au@16-s-16 nanoparticles upon biopolymer addition using the Hildebrand–Benesi approach [59,60]. According to this approach, the binding of a nanoparticle (Au) to a free biopolymer site (S) to produce an occupied site (AuS) can be expressed by the following reaction:

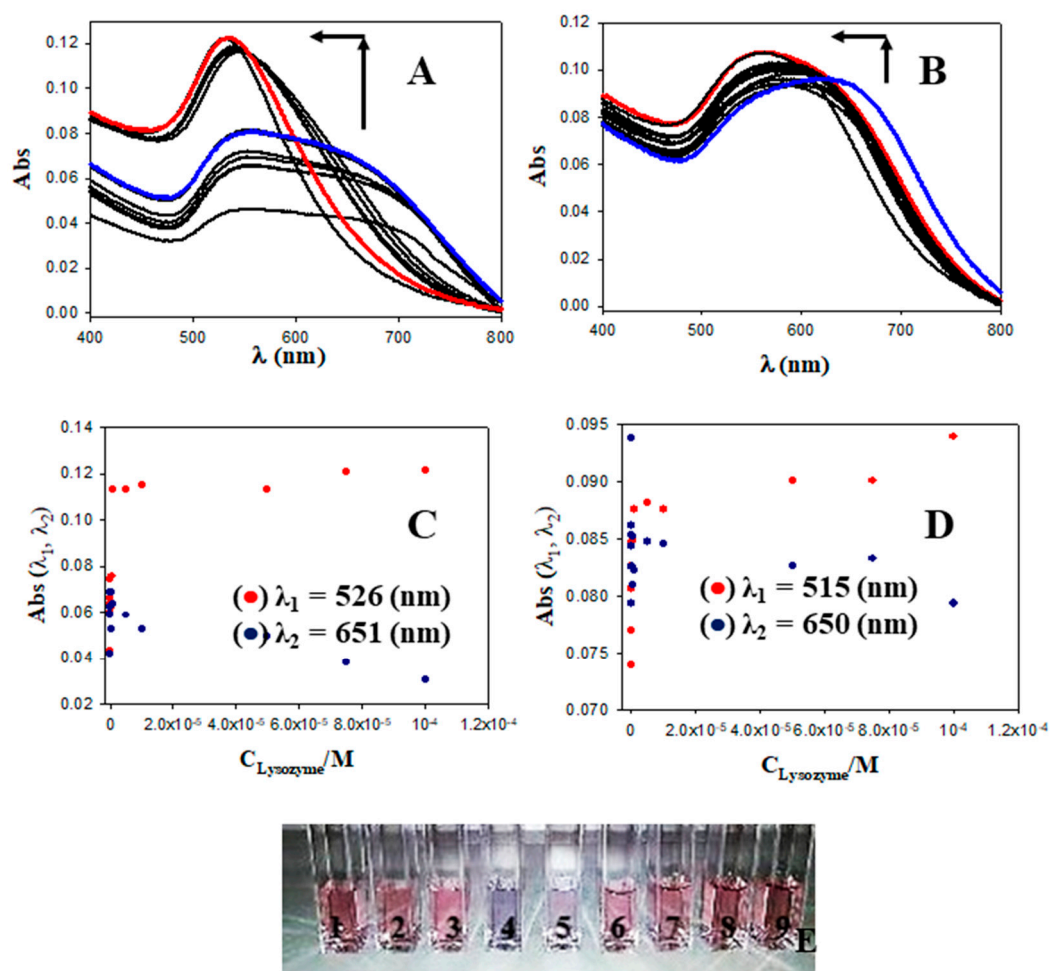


Figure 6. Absorbance titration of aggregated Au@16-s-16/SDS systems at different C_{Lysozyme} concentrations (addition method A). (A,B) $C_{\text{Lysozyme}} = 0 \mu\text{M}$ (blue spectrum), $C_{\text{Lysozyme}} = 100 \mu\text{M}$ (red spectrum), $C_{\text{Lysozyme}} = 0.001, 0.005, 0.01, 0.05, 0.50, 0.65, 1.00, 5.00, 10.0, 50.0$ and 75.0 and $100.0 \mu\text{M}$ (black spectrum, arrow direction). (C,D) Absorbance versus C_{Lysozyme} , red (nonaggregated nanoparticles) and blue points (aggregated nanoparticles) correspond to absorbance data at fixed wavelength. (E) Detailed view of corresponding color changes for Au@16-3-16/SDS/Lysozyme system. (1) $C_{\text{Lysozyme}} = 0 \mu\text{M}$, (2) $C_{\text{Lysozyme}} = 0.001$, (3) $C_{\text{Lysozyme}} = 0.005$, (4) $C_{\text{Lysozyme}} = 0.05$, (5) $C_{\text{Lysozyme}} = 1.0 \mu\text{M}$, (6) $C_{\text{Lysozyme}} = 10.0 \mu\text{M}$, (7) $C_{\text{Lysozyme}} = 50.0 \mu\text{M}$, (8) $C_{\text{Lysozyme}} = 75.0 \mu\text{M}$, and (9) $C_{\text{Lysozyme}} = 100.0 \mu\text{M}$.

Denoting the optical absorbance of the nanoparticle in the presence of biopolymer or SDS, the optical response in its absence, and the molar extinction coefficient of the

i-th species as *A*, *A*₀, and *ε*_{*i*}, respectively, it was shown that the concentrations of the gold nanoparticle/biopolymer complex and the free nanoparticle were: $[AuS] = (A - A_0) / (\epsilon_{AuS} - \epsilon_{Au}) = \Delta Abs / \Delta \epsilon$ and $[Au] = C_{Au} - [AuS]$, respectively. Consequently, both the equilibrium constant, defined as $K = [AuS] / ([Au] \times [S])$, and the value of the difference in the extinction coefficients of the nanocomplex and the nanoparticle, $\Delta \epsilon = \epsilon_{AuS} - \epsilon_{Au}$, can be evaluated from titration data using iterative fits to an extension of the Hildebrand–Benesi equation [78]:

$$\left(\frac{C_{Au} \times C_S}{\Delta Abs} + \frac{\Delta Abs}{\Delta \epsilon^2} \right) = \frac{1}{K \times \Delta \epsilon} + \left(\frac{C_{Au} + C_S}{\Delta \epsilon} \right) \quad (2)$$

The values of the binding constants for DNA/Au@16-s-16, Lysozyme/Au@16-s-16 and Au@16-s-16/SDS interactions calculated from Equation (2) are collected in Table 3; the curve fitting for distinct Au@16-s-16/biopolymer complexes is given in Figure S9.

Table 3. Equilibrium binding constants for the interaction among the reactants.

K (M ⁻¹)	Au@16-3-16	Au@16-6-16	SDS
DNA	$(1.2 \pm 0.5) \times 10^5$ (a)	$(5.1 \pm 0.5) \times 10^4$ (a)	– (b)
Lysozyme	$(8.40 \pm 0.04) \times 10^6$ (a)	$(9.0 \pm 0.5) \times 10^5$ (a)	514 (c)
SDS	$(2.5 \pm 0.2) \times 10^4$ (a)	$(1.21 \pm 0.13) \times 10^4$ (a)	

(a) Fit to Equation (2) of the absorbance data at the maximum of SPR band. (b) Estimation from reference [73]. (c) Data obtained from reference [75].

From these results, it can be observed that gold nanoparticle/biopolymer binding was highly favored for both biopolymers and the associated binding free energy of the interaction was more negative than that corresponding to the SDS/biopolymer interaction. It is important to note that the strength of the interaction was higher in the case of Lysozyme. This fact is in line with colorimetric results, in which DNA biopolymer exerted an important protective effect on SDS-induced Au@16-s-16 aggregation (see Figure 5). However, it does not explain the behavior of the nanosystem based on Lysozyme, in which it was necessary to add the biopolymer to the previously mixed Au@16-s-16/SDS complex (addition method A) to effectively accomplish the disaggregation processes. Thus, the explanation of such behavior could be related to biopolymer conformational changes and must be explored with other structural techniques. In this sense, we used the highly sensitive AFM technique to explore the existence and nature of possible conformational changes induced in the biomolecules. In particular, we selected the system configuration in which we observed complete disaggregation for each nanosystem according to the results described in Figures 5 and 6; taking into account the appropriate order of addition, the results are given in Figures 7 and 8. Figure 7A–C show that when the SDS surfactant was added to the Au@16-3-16/DNA mixture using method B, the APTES-modified mica surface was covered with a large-scale two-dimensional x-y DNA network. In these structures, biopolymer aggregation was mediated by cross-linking features and some condensation events were evident from the existence of globular condensates along the biopolymer chains. Moreover, bright dots coincident with DNA chains could be observed; their height in the z-direction was compatible with the size of the isolated Au@16-3-16, taking into account the typical DNA height in the z-direction. The mean size of the dots from the analysis of more than 200 particles measured in the z-direction was (4.8 ± 1.1) nm. This value can be directly compared with the size of Au@16-3-16 measured with TEM (3.8 ± 0.8) nm and the DNA heights in the z-direction, which had a mean value of 1.2 nm. Given the DNA deformation induced by the force applied to the AFM tip, the DNA height in the z-direction was somewhat smaller than the theoretical values of 2 nm, in accordance with Bustamante’s hypothesis [79]. The similarities between the sizes of the dots coincident with DNA chains suggests that the complexes observed in the z-direction were formed as a consequence of the highly favored Au@16-3-16/DNA interaction, and the gold nanoparticle’s multiple binding sites were easily exposed to the biopolymer. The situation was quite different for

the analogous 16-6-16-based nanosystem depicted in Figure 7D–F. That is, the presence of a large-scale DNA network in the x-y direction was replaced by the existence of large aggregates of about 20 nm and (10.3 ± 1.6) nm in the x-y and z-direction, respectively, in which some free DNA chains protruded outward. Moreover, some nanoparticles remained outside the nanocomplex. This fact suggests that the Au@16-6-16/DNA interaction and the distance between the nanoparticles along the DNA chains were not sufficient to maintain the stability of the DNA x-y network, and the biopolymer tended to collapse around Au@16-6-16-bound nanoparticles, forming the aggregates observed in the z-direction.

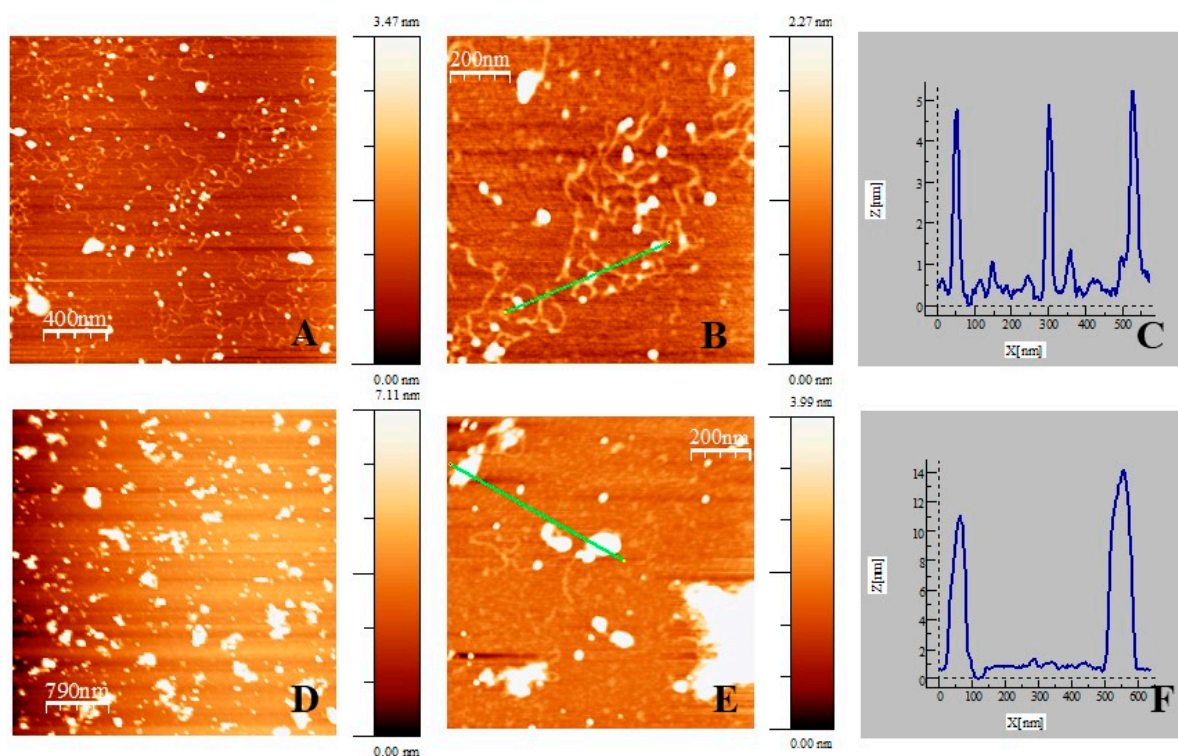


Figure 7. AFM topography images of Au@16-3-16/DNA/SDS and Au@16-6-16/DNA/SDS systems adsorbed on APTES-modified mica surface under Au@16-s-16 disaggregation conditions, and the corresponding size distribution of Au@16-s-16 nanoparticles along the selected lines. Reactant concentrations used were: $C_{\text{Au@16-3-16}} = 1.74 \times 10^{-8}$ M, $C_{\text{Au@16-6-16}} = 1.38 \times 10^{-8}$ M, $C_{\text{SDS}} = 30 \mu\text{M}$, and $C_{\text{DNA}} = 1.0 \times 10^{-5}$ M. (A–C) Au@16-3-16/DNA/SDS system. (D–F) Au@16-6-16/DNA/SDS system (addition method B).

In the case of the Lysozyme-based nanosystem, favorable lysozyme/SDS binding influenced the nature of the nanostructures observed. Figure 8 shows that given the size of the free Lysozyme proteins, with a particle size of around 2.5 nm [41] and a mean size of the free nanoparticles measured by TEM of less than 5 nm, it is clear that both Au@16-s-16/SDS/Lysozyme nanocomplexes originated aggregates in the z-direction. The size of the particles in the z-direction was very similar among the distinct nanostructures, with an average size of (10.3 ± 1.6) nm and (12.5 ± 1.8) nm for 16-3-16 and 16-6-16-based nanosystems, respectively. However, larger aggregates were observed from the AFM analysis, with a size of about 2 μm in the x-y direction in the case of the Au@16-6-16/SDS/Lysozyme nanosystem; these were much larger compared to the analogous 16-3-16-based nanosystem.

To verify the size of the nanostructures observed using AFM technique, we performed DLS experiments in the presence of biomolecules. The results obtained are given in Table 4 and Figure S10. The hydrodynamic values observed in the table reveal the existence of large x-y aggregates for Au@16-3-16/DNA/SDS and Au@16-6-16/SDS/Lysozyme nanosystems, respectively. Moreover, the progress of the Au@16-s-16/SDS disaggregation phenomena

with increasing biopolymer concentration could be observed when comparing the value of the hydrodynamic diameter in the absence of the biomolecule with those obtained at very low $C_{\text{biopolymer}}$ concentrations, in which the formation of such structures were still in an early stage (see Table 4).

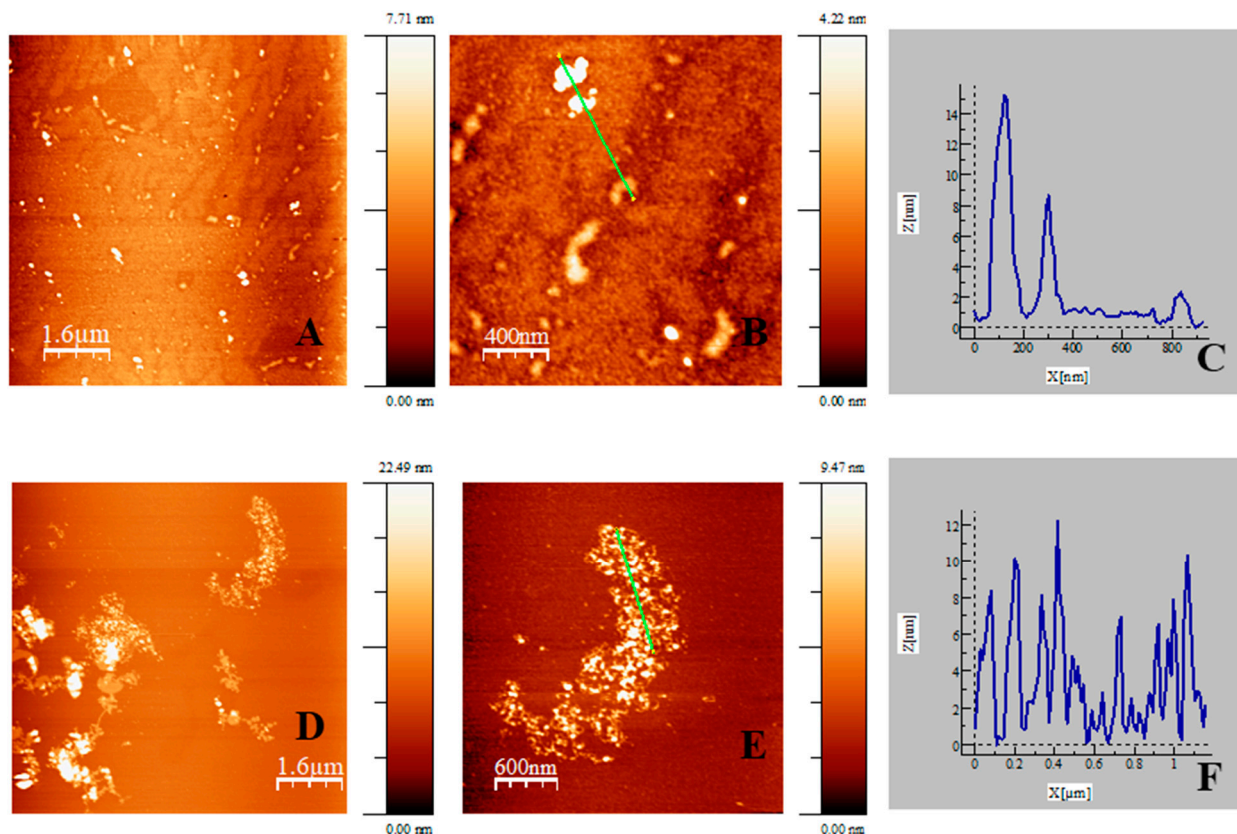


Figure 8. AFM topography images of Au@16-3-16/Lysozyme/SDS and Au@16-6-16/Lysozyme/SDS systems adsorbed on APTES-modified mica surface under Au@16-s-16 disaggregation condition, and the corresponding size distribution of Au@16-s-16 nanoparticles along the selected lines. Reactant concentrations used were: $C_{\text{Au@16-3-16}} = 1.74 \times 10^{-8}$ M, $C_{\text{Au@16-6-16}} = 1.38 \times 10^{-8}$ M, $C_{\text{SDS}} = 30 \mu\text{M}$, and $C_{\text{Lysozyme}} = 1.0 \times 10^{-5}$ M. (A–C) Au@16-3-16/SDS/Lysozyme system. (D–F) Au@16-6-16/SDS/Lysozyme system (addition method A).

Table 4. Values of the hydrodynamic diameters of different Au@16-s-16 nanosystems in the presence of fixed $C_{\text{SDS}} = 5.0 \times 10^{-5}$ M concentration and biomolecules.

$C_{\text{Biomolecule}}/\text{M}$	Au@16-3-16/Biopolymer/SDS	Au@16-6-16/Biopolymer/SDS
0	(748 ± 11) nm	(400 ± 12) nm
$C_{\text{DNA}} = 1.0 \times 10^{-6}$	$d_1 = (220 \pm 10)$ nm, 5% $d_2 = (43 \pm 5)$ nm, 95%	$d_1 = (106 \pm 14)$ nm, 2% $d_2 = (33 \pm 7)$ nm, 98%
$C_{\text{DNA}} = 5.0 \times 10^{-4}$	$d_1 = (450 \pm 6)$ nm, 96% $d_2 = (50 \pm 6)$ nm, 4%	(11.7 ± 1.3) nm
$C_{\text{Lysozyme}} = 5.0 \times 10^{-8}$	(615 ± 21) nm	$d_1 = (342 \pm 17)$ nm, 7% $d_2 = (79 \pm 3)$ nm, 93%
$C_{\text{Lysozyme}} = 1.0 \times 10^{-4}$	(44 ± 3) nm	(712 ± 14) nm

To summarize, distinct types of aggregates were observed for both DNA- and Lysozyme-based nanosystems: (i) a large-scale network in the x-y direction for the Au@16-3-16/DNA/SDS system without aggregation in the z-direction, (ii) small aggregates with an average size of 20 nm and 10.3 nm in the x-y and z directions, respectively, for the Au@16-6-16/DNA/SDS system, (iii) small aggregates in the z-direction of 10.3 nm in size for the

Au@16-3-16/SDS/Lysozyme nanosystem, and (iv) large aggregates of 12.5 and 2 μm in the z and x-y directions, respectively, for the Au@16-6-16/SDS/Lysozyme nanosystem.

However, there were certain similarities among the aggregates depending on the type of gemini surfactant that integrated into the nanosystem. Specifically, nanosystems based on 16-3-16 gemini surfactant were smaller in size in the z-direction, and the distance between the neighboring Au@16-3-16 nanoparticles was greater than in the case of the homologous 16-6-16 nanosystem. In fact, this special spatial distribution of the nanoparticles among the complexes could contribute to the differences in the absorbance response pattern observed in Figures 5 and 6, in which the amplitude of absorbance changes in the aggregate band was more evident for 16-3-16-based nanosystems in both biopolymers. On the other hand, focusing again on the type of surfactant used to functionalize the nanoparticle, it can also be noted that the 16-3-16 derivatives produced more stable Au@16-s-16/biopolymer complexes (see Table 3). Therefore, the strength of the binding Au@16-s-16/biopolymer, the nature of the aggregates, and the distance between the nanoparticles in the nanocomplexes could directly influence the aggregation state of the original nanosystem and, consequently, the sensitivity of the sensor. To correlate these aspects with the sensitivity of the sensor, the changes observed in the SPR experimental spectra of Au@16-s-16/SDS systems in the presence of biomolecules were analyzed in depth using deconvolution procedures (see Figure S11). The results are summarized in Tables 5 and 6.

Again, two characteristic bands were displayed when the deconvolution procedure was applied; one can be assigned to nonaggregated particles, designated λ_1 , and the other to aggregated nanosystems, designated λ_2 , which diminished as the $C_{\text{biopolymer}}$ increased in each case. Taking into account the values of the peak area assigned to each wavelength λ_1 and λ_2 , it seems evident that, at low biopolymer concentrations, the main contribution to the SPR band corresponded to the aggregated systems. Subsequently, the magnitude of the nonaggregated peak area gained importance until a certain concentration was reached, at which point a unique SPR band appeared.

Table 5. Deconvolution parameters obtained from Au@16-s-16 spectra in the presence of DNA and SDS following the addition method B (Au@16-s-16 + DNA + SDS). Gold nanoparticle and SDS concentrations were fixed in all experiments ($C_{\text{Au@16-3-16}} = 0.174 \text{ nM}$, $C_{\text{Au@16-6-16}} = 0.138 \text{ nM}$, and $C_{\text{SDS}} = 30 \mu\text{M}$).

Au@16-3-16/DNA			Au@16-6-16/DNA		
$C_{\text{DNA}} \text{ (M)}$	$\lambda_{1, \text{max}}/\text{nm}$ (Area ₁)	$\lambda_{2, \text{max}}/\text{nm}$ (Area ₂)	C_{DNA}/M	$\lambda_{1, \text{max}}/\text{nm}$ (Area ₁)	$\lambda_{2, \text{max}}/\text{nm}$ (Area ₂)
0	548 (1.94)	651 (10.17)	0	551 (1.82)	650 (10.84)
5.0×10^{-8}	548 (1.68)	642 (11.08)	5.0×10^{-8}	547 (1.87)	639 (10.01)
1.0×10^{-7}	545 (1.65)	640 (10.73)	1.0×10^{-7}	545 (1.70)	638 (10.15)
5.0×10^{-7}	544 (1.66)	638 (10.71)	5.0×10^{-7}	544 (1.73)	634 (9.51)
1.0×10^{-6}	543 (2.02)	620 (9.17)	7.5×10^{-7}	542 (1.71)	632 (9.93)
5.0×10^{-6} (*)	—	539	1.0×10^{-6}	542 (1.73)	629 (9.31)
			5.0×10^{-6}	—	538

(*) Data specification for the first concentration at which the deconvolution process is not necessary for each system.

Table 6. Deconvolution parameters obtained from Au@16-s-16 spectra in the presence of Lysozyme and SDS following the addition method A. Gold nanoparticle and SDS concentrations were fixed in all experiments ($C_{\text{Au@16-3-16}} = 0.174 \text{ nM}$, $C_{\text{Au@16-6-16}} = 0.138 \text{ nM}$, and $C_{\text{SDS}} = 30 \mu\text{M}$).

Au@16-3-16/Lysozyme			Au@16-6-16/Lysozyme		
$C_{\text{Lysozyme}} \text{ (M)}$	$\lambda_{1, \text{max}}/\text{nm}$ (Area ₁)	$\lambda_{2, \text{max}}/\text{nm}$ (Area ₂)	$C_{\text{Lysozyme}}/\text{M}$	$\lambda_{1, \text{max}}/\text{nm}$ (Area ₁)	$\lambda_{2, \text{max}}/\text{nm}$ (Area ₂)
0	548 (1.94)	651 (10.17)	0	551 (1.82)	650 (10.84)
1.0×10^{-9}	545 (1.92)	640 (12.83)	1.0×10^{-9}	547 (1.71)	637 (10.44)

Table 6. Cont.

Au@16-3-16/Lysozyme			Au@16-6-16/Lysozyme		
$C_{\text{Lysozyme}}(\text{M})$	$\lambda_{1, \text{max}}/\text{nm}$ (Area ₁)	$\lambda_{2, \text{max}}/\text{nm}$ (Area ₂)	$C_{\text{Lysozyme}}/\text{M}$	$\lambda_{1, \text{max}}/\text{nm}$ (Area ₁)	$\lambda_{2, \text{max}}/\text{nm}$ (Area ₂)
5.0×10^{-9}	545 (1.96)	639 (9.20)	5.0×10^{-9}	543 (1.71)	629 (9.18)
1.0×10^{-8}	545 (2.06)	637 (10.60)	7.5×10^{-9}	541 (1.86)	628 (9.36)
5.0×10^{-8}	544 (2.47)	631 (8.50)	1.0×10^{-8}	542 (1.76)	627 (9.21)
1.0×10^{-7}	543 (2.27)	623 (8.92)	5.0×10^{-8}	541 (1.73)	625 (9.44)
5.0×10^{-7} (*)	—	553	1.0×10^{-7}	541 (1.78)	624 (9.62)
			5.0×10^{-7}	541 (1.68)	616 (8.47)
			1.0×10^{-6}	539 (1.70)	614 (7.07)
			5.0×10^{-6}	534 (1.84)	604 (7.21)
			1.0×10^{-5} (*)	—	586

(*) Data specification for the first concentration at which the deconvolution process is not necessary for each system.

As illustrated in Figure 9, the plots of $\ln(1/\Delta\lambda_2)$ vs. $\ln(C_{\text{biopolymer}}/\Delta\lambda_2)$ gave a linear calibration curve for all the nanosystems regardless of the surfactant used or the biopolymer detected.

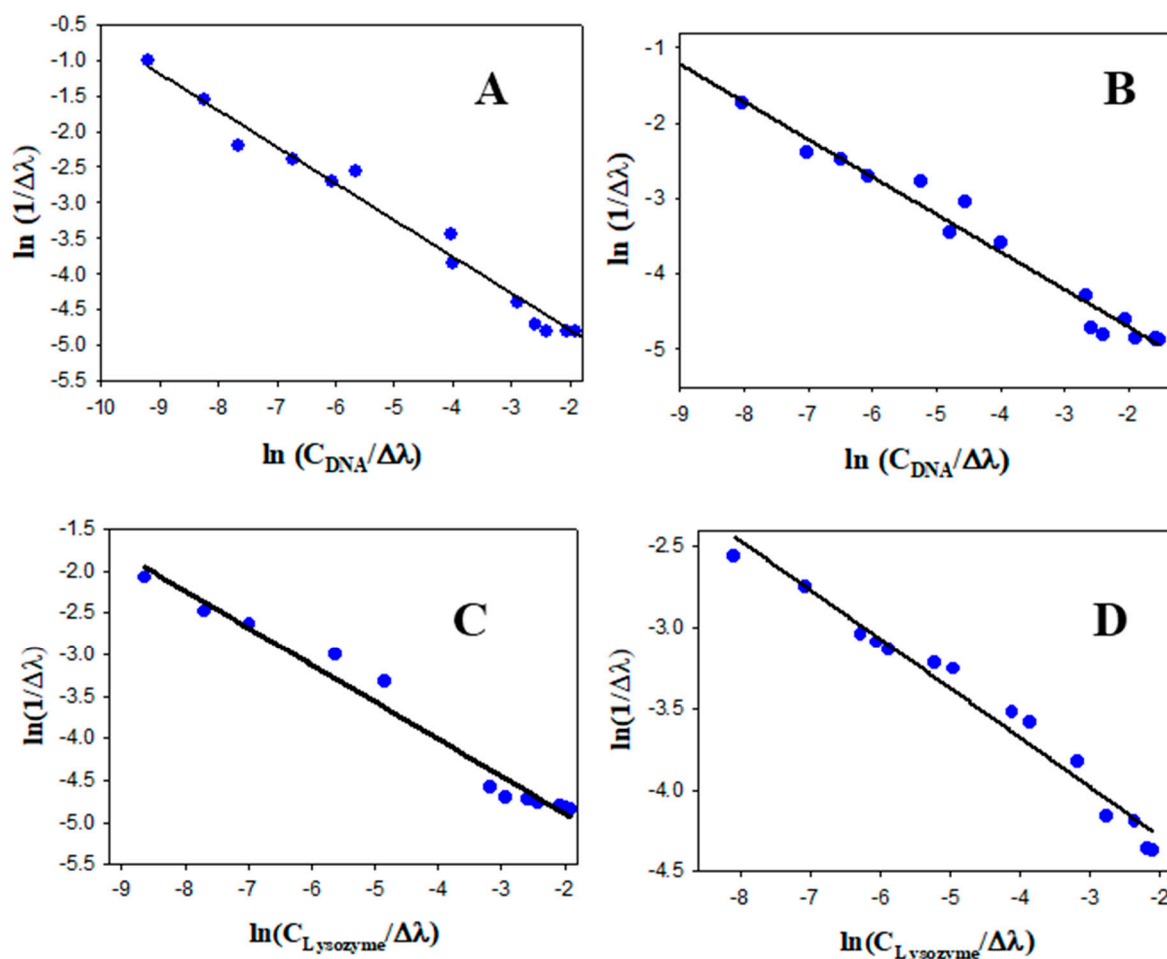


Figure 9. Colorimetric response patterns obtained with colorimetric sensors in water, showing the linear relationship between $1/\Delta\lambda_2$ logarithms and the logarithms of the quotient between biopolymer concentration and $\Delta\lambda_2$. (A) Au@16-3-16/SDS/DNA system. (B) Au@16-6-16/SDS/DNA system. (C) Au@16-3-16/SDS/Lysozyme system. (D) Au@16-6-16/SDS/Lysozyme system.

The analytical method developed in water media was validated using horse serum media to assess the possible matrix effect in the sensor response. Figure 10 shows the plot of $\ln(1/\Delta\lambda_2)$ vs. $\ln(C_{\text{biopolymer}}/\Delta\lambda_2)$, giving a linear response in the same range of concentrations verified in water for all the studied nanosystems. These results support the selectivity and validity of the method due to the presence of multiple components in the serum media that can act as possible interferences in the measurement process.

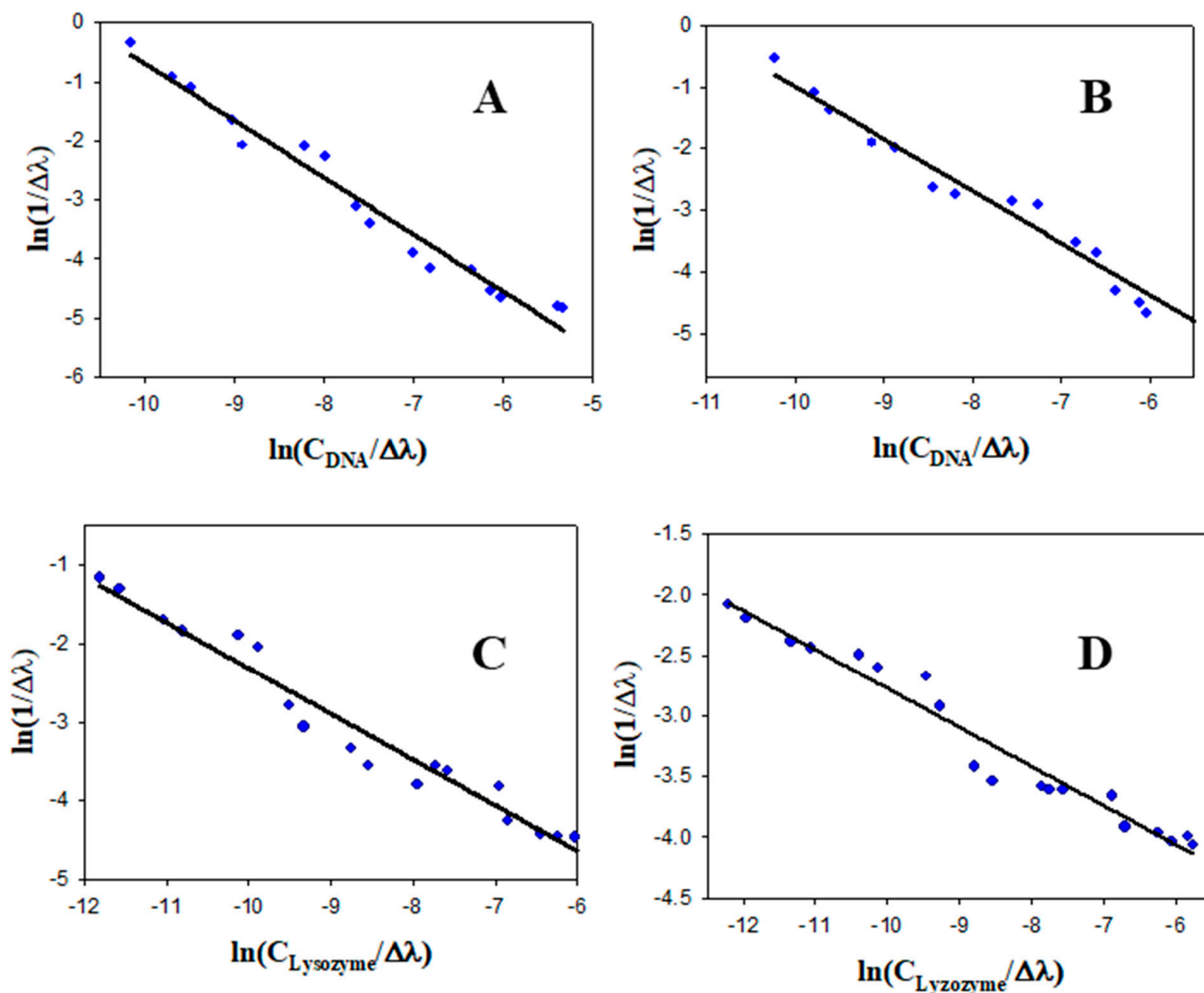


Figure 10. Colorimetric response patterns obtained with colorimetric sensors in horse serum media, showing the linear relationship between $1/\Delta\lambda_2$ logarithms and the logarithms of the quotient between biopolymer concentration and $\Delta\lambda_2$. (A) Au@16-3-16/SDS/DNA system. (B) Au@16-6-16/SDS/DNA system. (C) Au@16-3-16/SDS/Lysozyme system. (D) Au@16-6-16/SDS/Lysozyme system.

However, looking at the values of the ordinate (y_0) and the slope (m) of the curves collected in Table 7, it is clear that the specific colorimetric response was distinct for each nanosystem and the type of media used, in such a way that given the slope values, the best sensitivity was obtained for the Au@16-3-16/DNA/SDS nanosystem (see Figures 9A and 10A), and in general, when the 16-3-16 gemini surfactant was used. Moreover, the detection limit (LOD) and quantification limit (LOQ) values were calculated as $\text{LOD} = 3.3 \times \sigma/m$ and $\text{LOQ} = 10 \times \sigma/m$, where σ is the standard deviation of the response [80].

Table 7. Values for limit of detection (LOD), limit of quantitation (LOQ), and linear regression parameters (slope = m and y intercept = y_0 and standard deviation = SD) for DNA and Lysozyme quantification based on colorimetric response obtained from data in Figures 9 and 10.

System	m	y_0	SD	LOD	LOQ
Au@16-3-16/DNA/SDS (water)	-0.519 ± 0.02	-5.80 ± 0.10	0.194	8 nM	24 nM
Au@16-6-16/DNA/SDS (water)	-0.498 ± 0.02	-0.570 ± 0.10	0.198	9 nM	27 nM
Au@16-3-16/SDS/Lysozyme (water)	-0.44 ± 0.02	-5.77 ± 0.11	0.185	0.12 nM	0.37 nM
Au@16-6-16/SDS/Lysozyme (water)	-0.304 ± 0.017	-4.89 ± 0.08	0.109	8.5 pM	25.7 pM
Au@16-3-16/DNA/SDS (horse serum)	-0.966 ± 0.05	-10.4 ± 0.30	0.230	0.24 nM	0.73 nM
Au@16-6-16/DNA/SDS (horse serum)	-0.846 ± 0.04	-9.45 ± 0.30	0.240	0.50 nM	1.52 nM
Au@16-3-16/SDS/Lysozyme (horse serum)	-0.581 ± 0.03	-8.51 ± 0.25	0.140	3.1 pM	9.5 pM
Au@16-6-16/SDS/Lysozyme (horse serum)	-0.322 ± 0.015	-5.99 ± 0.14	0.143	3.5 pM	11 pM

Taking into account these values for each nanosystem, again, the colorimetric response suitability was presented in the following order: Au@16-3-16/SDS/Lysozyme > Au@16-6-16/SDS/Lysozyme > Au@16-3-16/DNA/SDS > Au@16-6-16/DNA/SDS. As a result, the Au@16-3-16-based nanosystem presented a better sensing response for each biopolymer studied here. Finally, a comment about the variation in the sensor response in the presence of horse serum seems to be pertinent. Note that some of the serum components were even biomolecules of high molecular weight such as gamma globulin, lactose dehydrogenase, or albumin. Additionally, there were other smaller biomolecules such as creatinine or bilirubin that could also interfere in the measurement. However, we demonstrated that if the concentration of serum is fixed in the measurement, the sensor response varies but retains its linearity in the same range of DNA and Lysozyme concentrations, supporting the validity of the method. Thus, correlating the colorimetric response with the thermodynamic and structural features analyzed at the beginning of this section, we can conclude that: (i) the greater the biopolymer–nanoparticle interaction is, the better the sensor response obtained; (ii) if the biopolymer/SDS interaction is negligible, it is better to add the biopolymer to the mixed Au@16-s-16/SDS complex according to addition method A; (iii) the presence of larger aggregates in the z-direction is unfavorable for the sensitivity of the method; (iv) the higher the interparticle distance in the nanocomplex is, the better the sensor response and sensitivity obtained. Note that maximum nanoparticle separation was obtained in the specific case of the formation of cross-linking aggregates in the x-y direction.

4. Conclusions

Biopolymer sensing was controlled following Au@16-s-16/DNA/SDS or Au@16-s-16/Lysozyme/SDS complex disaggregation using the UV-visible spectroscopic technique. The disaggregation procedure was accompanied by changes in the SPR band and color changes from blue to red that were visible to the naked eye, with a limit of detection in the picomolar range for lysozyme sensing.

Thermodynamic and structural studies using UV-visible spectroscopy, DLS, and AFM techniques served to gain insight into better nanosystem configuration, in which factors such as favorable Au@16-s-16/biopolymer binding, the absence of z-aggregates, and the interparticle distance among nanoparticles in aggregates are key parameters to be optimized and controlled for a better sensor response. In this sense, a better linear response was observed for both Au@16-3-16/DNA/SDS and Au@16-3-6/SDS/Lysozyme nanosystems, highlighting, from a structural perspective, the formation of cross-linking aggregates that favor both the distance between nanoparticles in the complexes and the absence of z-aggregates. These facts demonstrated that controlling the structural and binding features among the components of the nanosensor is crucial for the effective sensing of biomolecules using colorimetric methods.

Finally, the colorimetric method developed was shown to be simpler, faster, and more sensitive compared to other previously reported colorimetric, fluorimetry, mass spectrometry, chromatography, gel electrophoresis, and electrochemical methods. Moreover, the new

approach resolves problems associated with time lapse determination, especially in the case of Lysozyme, which usually requires a long incubation period for sample quantification.

Supplementary Materials: The following supporting information can be downloaded at: <https://www.mdpi.com/article/10.3390/chemosensors11040207/s1>, Figure S1: TEM images and size distribution of Au@16-s-16 nanoparticles in water. Figure S2: EDS spectra for Au@16-s-16/SDS complexes. Figure S3: Intensity versus position profiles for Au@16-s-16/SDS complexes showing the d spacing among gold atoms. Figure S4: Changes in maximum SPR wavelength as a function of CSDS concentration for the Au@16-3-16/SDS system, and associated color changes. Figure S5: Changes in the maximum SPR wavelength as a function of CSDS concentration for the Au@16-6-16/SDS system, and associated color changes. Figure S6: Absorbance titration of the Au@16-6-16/SDS system and its corresponding absorbance intensities versus CSDS concentrations. Figure S7: DLS results for Au@16-s-16/SDS complexes. Figure S8: Absorbance titration of aggregated Au@16-s-16/SDS systems at different C_{biopolymer} concentrations, showing irreversible aggregation processes. Figure S9: Analysis of the absorbance titration data according to the Hildebrand–Benesi model for Au@16-s-16/biopolymer systems in water. Figure S10: DLS results for Au@16-s-16/SDS complexes in the presence of biomolecules. Figure S11: Example of deconvolution of experimental SPR spectra obtained using Method B at three different C_{DNA} concentrations. Table S1: Values of the CMC of 16-s-16 gemini surfactants obtained by the surface tension technique and their comparison with other values reported in the bibliography.

Author Contributions: All authors had full access to all the data in the study and take responsibility for the integrity of the data and the accuracy of the data analysis. Conceptualization, supervision, formal analysis, methodology, and data curation, E.G. and R.M.G.-P.; visualization, E.G.; investigation, E.G., R.M.G.-P., R.P.-G. and E.K.; writing the original draft, E.G.; writing—review and editing, E.G. and R.M.G.-P.; funding acquisition, E.G. and R.P.-G. All authors have read and agreed to the published version of the manuscript.

Funding: This work was financed by the Consejería de Economía, Conocimiento, Empresa y Universidad of Junta de Andalucía (2021/FQM-386) and by VI PP USO SSGG (2021/00001297) and VII PP USO SSGG (2022/00000274) of the University of Seville.

Institutional Review Board Statement: Not applicable.

Informed Consent Statement: Not applicable.

Data Availability Statement: The data are contained within the article or Supplementary Materials.

Acknowledgments: The authors are grateful to the Microscopy and Functional Characterization Service of the Research, Technology and Innovation Center of the University of Seville (CITIUS).

Conflicts of Interest: The authors declare no conflict of interest. The Chemtra company had no role in the design of the study; in the collection, analyses, or interpretation of data; in the writing of the manuscript; or in the decision to publish the results.

References

1. Abhilash, M.; Thomas, D. Biopolymers for Biocomposites and Chemical Sensor Applications. In *Biopolymer Composites in Electronics*; Elsevier: Amsterdam, The Netherlands, 2017; pp. 405–435; ISBN 9780081009741.
2. Li, F.; Mahon, A.R.; Barnes, M.A.; Feder, J.; Lodge, D.M.; Hwang, C.-T.; Schafer, R.; Ruggiero, S.T.; Tanner, C.E. Quantitative and Rapid DNA Detection by Laser Transmission Spectroscopy. *PLoS ONE* **2011**, *6*, e29224. [[CrossRef](#)] [[PubMed](#)]
3. Bailey, V.J.; Easwaran, H.; Zhang, Y.; Griffiths, E.; Belinsky, S.A.; Herman, J.G.; Baylin, S.B.; Carraway, H.E.; Wang, T.-H. MS-QFRET: A Quantum Dot-Based Method for Analysis of DNA Methylation. *Genome Res.* **2009**, *19*, 1455–1461. [[CrossRef](#)]
4. Zhang, H.; Li, F.; Dever, B.; Wang, C.; Li, X.-F.; Le, X.C. Assembling DNA through Affinity Binding to Achieve Ultrasensitive Protein Detection. *Angew. Chem. Int. Ed.* **2013**, *52*, 10698–10705. [[CrossRef](#)]
5. Levinson, S.S.; Elin, R.J.; Yam, L. Light Chain Proteinuria and Lysozymuria in a Patient with Acute Monocytic Leukemia. *Clin. Chem.* **2002**, *48*, 1131–1132. [[CrossRef](#)]
6. Serra, C.; Vizoso, F.; Alonso, L.; Rodríguez, J.C.; González, L.O.; Fernández, M.; Lamelas, M.L.; Sánchez, L.M.; García-Muñiz, J.L.; Baltasar, A.; et al. Expression and Prognostic Significance of Lysozyme in Male Breast Cancer. *Breast Cancer Res.* **2002**, *4*, R16. [[CrossRef](#)] [[PubMed](#)]
7. Osserman, E.F.; Lawlor, D.P. Serum and Urinary Lysozyme (Muramidase) in Monocytic and Monomyelocytic Leukemia. *J. Exp. Med.* **1966**, *124*, 921–952. [[CrossRef](#)]

8. Noble, R.E.; Fudenberg, H.H. Leukocyte Lysozyme Activity in Myelocytic Leukemia. *Blood* **1967**, *30*, 465–473. [[CrossRef](#)]
9. Pruzanski, W.; Platts, M.E. Serum and Urinary Proteins, Lysozyme (Muramidase), and Renal Dysfunction in Mono- and Myelomonocytic Leukemia. *J. Clin. Investig.* **1970**, *49*, 1694–1708. [[CrossRef](#)] [[PubMed](#)]
10. Bodansky, O. The Leukemias and Lymphomas. In *Biochemistry of Human Cancer*; Academic Press: Cambridge, MA, USA, 1975; pp. 232–271; ISBN 978-0-12-109850-6.
11. Moe, P.J.; Haneberg, B.; Finne, P. Serum Lysozyme Activity in Children with Hematological and Malignant Disorders. *Acta Paediatr.* **1975**, *64*, 830–832. [[CrossRef](#)]
12. Bener, M.; Şen, F.B.; Kaşgöz, A.; Apak, R. Carrageenan-Based Colorimetric Sensor for Total Antioxidant Capacity Measurement. *Sens. Actuators B Chem.* **2018**, *273*, 439–447. [[CrossRef](#)]
13. Lin, T.-W.; Wu, H.-Y.; Tasi, T.-T.; Lai, Y.-H.; Shen, H.-H. Surface-Enhanced Raman Spectroscopy for DNA Detection by the Self-Assembly of Ag Nanoparticles onto Ag Nanoparticle–Graphene Oxide Nanocomposites. *Phys. Chem. Chem. Phys.* **2015**, *17*, 18443–18448. [[CrossRef](#)] [[PubMed](#)]
14. Liu, Q.; Pu, Z.; Asiri, A.M.; Al-Youbi, A.O.; Sun, X. Polydopamine Nanospheres: A Biopolymer-Based Fluorescent Sensing Platform for DNA Detection. *Sens. Actuators B Chem.* **2014**, *191*, 567–571. [[CrossRef](#)]
15. Wang, P.; Wilson, S.R. Mass Spectrometry-Based Protein Identification by Integrating de Novo Sequencing with Database Searching. *BMC Bioinform.* **2013**, *14* (Suppl. S2), S24. [[CrossRef](#)]
16. Stuting, H.H.; Krull, I.S. Complete On-Line Determination of Biopolymer Molecular Weight via High-Performance Liquid Chromatography Coupled to Low-Angle Laser Light Scattering, Ultraviolet, and Differential Refractive Index Detection. *Anal. Chem.* **1990**, *62*, 2107–2114. [[CrossRef](#)]
17. Chen, W.; Xu, D.; Liu, L.; Peng, C.; Zhu, Y.; Ma, W.; Bian, A.; Li, Z.; Yuan, Y.; Jin, Z.; et al. Ultrasensitive Detection of Trace Protein by Western Blot Based on POLY-Quantum Dot Probes. *Anal. Chem.* **2009**, *81*, 9194–9198. [[CrossRef](#)]
18. Shen, H.; Qu, F.; Xia, Y.; Jiang, X. Straightforward and Ultrastable Surface Modification of Microfluidic Chips with Norepinephrine Bitartrate Improves Performance in Immunoassays. *Anal. Chem.* **2018**, *90*, 3697–3702. [[CrossRef](#)]
19. Hassan, R.A.; Heng, L.Y.; Tan, L.L. Novel DNA Biosensor for Direct Determination of Carrageenan. *Sci. Rep.* **2019**, *9*, 6379. [[CrossRef](#)] [[PubMed](#)]
20. Tansil, N.C.; Gao, Z. Nanoparticles in Biomolecular Detection. *Nano Today* **2006**, *1*, 28–37. [[CrossRef](#)]
21. Sapkota, K.; Dhakal, S. FRET-Based Aptasensor for the Selective and Sensitive Detection of Lysozyme. *Sensors* **2020**, *20*, 914. [[CrossRef](#)]
22. Selsted, M.E.; Martinez, R.J. A Simple and Ultrasensitive Enzymatic Assay for the Quantitative Determination of Lysozyme in the Picogram Range. *Anal. Biochem.* **1980**, *109*, 67–70. [[CrossRef](#)]
23. Lou, T.; Qiang, H.; Chen, Z. Core-Shell Cu@Au Nanoparticles-Based Colorimetric Aptasensor for the Determination of Lysozyme. *Talanta* **2017**, *163*, 132–139. [[CrossRef](#)]
24. Moyano, D.F.; Rana, S.; Bunz, U.H.F.; Rotello, V.M. Gold Nanoparticle-Polymer/Biopolymer Complexes for Protein Sensing. *Faraday Discuss* **2011**, *152*, 33–120. [[CrossRef](#)]
25. Lynch, I.; Dawson, K.A. Protein-Nanoparticle Interactions. *Nano Today* **2008**, *3*, 40–47. [[CrossRef](#)]
26. Nisar, S.; Chansi; Mathur, A.; Basu, T.; Singh, K.R.B.; Singh, J. Template Free Anisotropically Grown Gold Nanocluster Based Electrochemical Immunosensor for Ultralow Detection of Cardiac Troponin I. *Biosensors* **2022**, *12*, 1144. [[CrossRef](#)]
27. Li, Y.; Qian, Z.; Shen, C.; Gao, Z.; Tang, K.; Liu, Z.; Chen, Z. Colorimetric Sensors for Alkaloids Based on the Etching of Au@MnO₂ Nanoparticles and MnO₂ Nanostars. *ACS Appl. Nano Mater.* **2021**, *4*, 8465–8472. [[CrossRef](#)]
28. Tang, L.; Li, J. Plasmon-Based Colorimetric Nanosensors for Ultrasensitive Molecular Diagnostics. *ACS Sens.* **2017**, *2*, 857–875. [[CrossRef](#)] [[PubMed](#)]
29. Zhang, Y.; McKelvie, I.D.; Cattrall, R.W.; Kolev, S.D. Colorimetric Detection Based on Localised Surface Plasmon Resonance of Gold Nanoparticles: Merits, Inherent Shortcomings and Future Prospects. *Talanta* **2016**, *152*, 410–422. [[CrossRef](#)]
30. Zhou, S.; Liang, D.; Burger, C.; Yeh, F.; Chu, B. Nanostructures of Complexes Formed by Calf Thymus DNA Interacting with Cationic Surfactants. *Biomacromolecules* **2004**, *5*, 1256–1261. [[CrossRef](#)] [[PubMed](#)]
31. Sato, K.; Hosokawa, K.; Maeda, M. Rapid Aggregation of Gold Nanoparticles Induced by Non-Cross-Linking DNA Hybridization. *J. Am. Chem. Soc.* **2003**, *125*, 8102–8103. [[CrossRef](#)] [[PubMed](#)]
32. Elghanian, R.; Storhoff, J.J.; Mucic, R.C.; Letsinger, R.L.; Mirkin, C.A. Selective Colorimetric Detection of Polynucleotides Based on the Distance-Dependent Optical Properties of Gold Nanoparticles. *Science* **1997**, *277*, 1078–1081. [[CrossRef](#)]
33. Kreibig, U.; Genzel, L. Optical Absorption of Small Metallic Particles. *Surf. Sci.* **1985**, *156*, 678–700. [[CrossRef](#)]
34. Weitz, D.A.; Huang, J.S.; Lin, M.Y.; Sung, J. Limits of the Fractal Dimension for Irreversible Kinetic Aggregation of Gold Colloids. *Phys. Rev. Lett.* **1985**, *54*, 1416–1419. [[CrossRef](#)]
35. Kallay, N.; Žalac, S. Stability of Nanodispersions: A Model for Kinetics of Aggregation of Nanoparticles. *J. Colloid. Interface Sci.* **2002**, *253*, 70–76. [[CrossRef](#)]
36. Liao, J.; Zhang, Y.; Yu, W.; Xu, L.; Ge, C.; Liu, J.; Gu, N. Linear Aggregation of Gold Nanoparticles in Ethanol. *Colloids. Surf. A Phys. Eng. Asp.* **2003**, *223*, 177–183. [[CrossRef](#)]
37. Prasher, R.; Phelan, P.E.; Bhattacharya, P. Effect of Aggregation Kinetics on the Thermal Conductivity of Nanoscale Colloidal Solutions (Nanofluid). *Nano Lett.* **2006**, *6*, 1529–1534. [[CrossRef](#)]

38. Pamies, R.; Cifre, J.G.H.; Espín, V.F.; Collado-González, M.; Baños, F.G.D.; de La Torre, J.G. Aggregation Behaviour of Gold Nanoparticles in Saline Aqueous Media. *J. Nanoparticle Res.* **2014**, *16*, 2376. [[CrossRef](#)]
39. Iglesias, E.; Prado-Gotor, R. Interaction of Gold Nanoparticles Mediated by Captopril and S-Nitrosocaptopril: The Effect of Manganese Ions in Mild Acid Medium. *Phys. Chem. Chem. Phys.* **2015**, *17*, 644–654. [[CrossRef](#)] [[PubMed](#)]
40. Bahram, M.; Madrakian, T.; Alizadeh, S. Simultaneous Colorimetric Determination of Morphine and Ibuprofen Based on the Aggregation of Gold Nanoparticles Using Partial Least Square. *J. Pharm. Anal.* **2017**, *7*, 411–416. [[CrossRef](#)]
41. Grueso, E.; Giráldez-Pérez, R.M.; Kuliszewska, E.; Guerrero, J.A.; Prado-Gotor, R. Reversible Cationic Gemini Surfactant-Induced Aggregation of Anionic Gold Nanoparticles for Sensing Biomolecules. *Colloids. Surf. A Phys. Eng. Asp.* **2021**, *610*, 125893. [[CrossRef](#)]
42. Rogowski, J.L.; Verma, M.S.; Gu, F.X. Discrimination of Proteins Using an Array of Surfactant-Stabilized Gold Nanoparticles. *Langmuir* **2016**, *32*, 7621–7629. [[CrossRef](#)] [[PubMed](#)]
43. Vasilescu, A.; Wang, Q.; Li, M.; Boukherroub, R.; Szunerits, S. Aptamer-Based Electrochemical Sensing of Lysozyme. *Chemosensors* **2016**, *4*, 10. [[CrossRef](#)]
44. Grueso, E.; Giráldez-Pérez, R.M.; Prado-Gotor, R. Recent Advances in the Design of Colorimetric Sensors Based on Gold Nanoparticles. In *Advanced Nanomaterials*; Ikhmayies, S.J., Ed.; Springer International Publishing: Cham, Switzerland, 2022; pp. 445–495; ISBN 978-3-031-11996-5.
45. Serrano, V.M.; Silva, I.S.P.; Cardoso, A.R.; Sales, M.G.F. Carbon Electrodes with Gold Nanoparticles for the Electrochemical Detection of MiRNA 21-5p. *Chemosensors* **2022**, *10*, 189. [[CrossRef](#)]
46. Yu, L.; Li, N. Noble Metal Nanoparticles-Based Colorimetric Biosensor for Visual Quantification: A Mini Review. *Chemosensors* **2019**, *7*, 53. [[CrossRef](#)]
47. Yao, X.; Ma, X.; Ding, C.; Jia, L. Colorimetric Determination of Lysozyme Based on the Aggregation of Gold Nanoparticles Controlled by a Cationic Polymer and an Aptamer. *Microchim. Acta* **2016**, *183*, 2353–2359. [[CrossRef](#)]
48. Castillo, P.M.; Fernández-Acejo, F.J.; Carnerero, J.M.; Prado-Gotor, R.; Jimenez-Ruiz, A. Colorimetric, Naked-Eye Detection of Lysozyme in Human Urine with Gold Nanoparticles. *Nanomaterials* **2021**, *11*, 612. [[CrossRef](#)]
49. Kanjanawarut, R.; Su, X. Colorimetric Detection of DNA Using Unmodified Metallic Nanoparticles and Peptide Nucleic Acid Probes. *Anal. Chem.* **2009**, *81*, 6122–6129. [[CrossRef](#)]
50. Sato, K.; Hosokawa, K.; Maeda, M. Non-Cross-Linking Gold Nanoparticle Aggregation as a Detection Method for Single-Base Substitutions. *Nucleic. Acids Res.* **2005**, *33*, e4. [[CrossRef](#)] [[PubMed](#)]
51. Sambrook, J.; Fritsch, E.F.; Maniatis, T. *Molecular Cloning: A Laboratory Manual.*; Cold Spring Harbor Laboratory Press: Cold Spring Harbor, NY, USA, 1989; ISBN 0879693096.
52. Secco, F.; Venturini, M.; Biver, T.; Sánchez, F.; Prado-Gotor, R.; Grueso, E. Solvent Effects on the Kinetics of the Interaction of 1- Pyrenecarboxaldehyde with Calf Thymus DNA. *J. Phys. Chem. B* **2010**, *114*, 4686–4691. [[CrossRef](#)]
53. Felsenfeld, G.; Hirschman, S.Z. A Neighbor-Interaction Analysis of the Hypochromism and Spectra of DNA. *J. Mol. Biol.* **1965**, *13*, 407–427. [[CrossRef](#)] [[PubMed](#)]
54. Kuliszewska, E.; Brecker, L. Gemini Surfactants Foam Formation Ability and Foam Stability Depends on Spacer Length. *J. Surfactants Deterg.* **2014**, *17*, 951–957. [[CrossRef](#)]
55. Pozniatek, B.P.; Kuliszewska, E. Competition between Substitution and Elimination Reaction Channels from Fragmentation Ratios of Diquaternary Ammonium Bromide and Formate Ion Pairs. *Int. J. Mass Spectrom.* **2013**, *348*, 29–38. [[CrossRef](#)]
56. Zana, R.; Benraou, M.; Rueff, R. Alkanediyl- α,ω -Bis(Dimethylalkylammonium Bromide) Surfactants. 1. Effect of the Spacer Chain Length on the Critical Micelle Concentration and Micelle Ionization Degree. *Langmuir* **1991**, *7*, 1072–1075. [[CrossRef](#)]
57. Giráldez-Pérez, R.M.; Grueso, E.; Lhamyani, S.; Perez-Tejeda, P.; Gentile, A.M.; Kuliszewska, E.; Roman-Perez, J.; el Bekay, R. MiR-21/Gemini Surfactant-Capped Gold Nanoparticles as Potential Therapeutic Complexes: Synthesis, Characterization and in Vivo Nanotoxicity Probes. *J. Mol. Liq.* **2020**, *313*, 113577. [[CrossRef](#)]
58. Cheng, H.-W.; Skeete, Z.R.; Crew, E.R.; Shan, S.; Luo, J.; Zhong, C.-J. Chapter 2—Synthesis of Gold Nanoparticles. In *Comprehensive Analytical Chemistry*; Valcárcel, M., López-Lorente, Á.I., Eds.; Elsevier: Amsterdam, The Netherlands, 2014; Volume 66, pp. 37–79; ISBN 0166-526X.
59. Benesi, H.A.; Hildebrand, J.H. A Spectrophotometric Investigation of the Interaction of Iodine with Aromatic Hydrocarbons. *J. Am. Chem. Soc.* **1949**, *71*, 2703–2707. [[CrossRef](#)]
60. Hynes, M.J.; Diebler, H. The Binding of Ni²⁺ to Adenylyl-3',5'-Adenosine and to Poly(Adenylic Acid). *Biophys. Chem.* **1982**, *16*, 79–88. [[CrossRef](#)]
61. Wojdyr, M. Fityk: A General-Purpose Peak Fitting Program. *J. Appl. Cryst.* **2010**, *43*, 1126–1128. [[CrossRef](#)]
62. Yang, C.-S.; Shih, M.-S.; Chang, F.-Y. Evolution Study of Photo-Synthesized Gold Nanoparticles by Spectral Deconvolution Model: A Quantitative Approach. *New J. Chem.* **2006**, *30*, 729–735. [[CrossRef](#)]
63. Prado-Gotor, R.; Jimenez-Ruiz, A.; Carnerero, J.M.; Grueso, E.; Villa, I. CIELab Chromaticity Evolution to Measure the Binding Free Energy of Non-Colored Biomolecules to Gold Nanoparticles. *RSC Adv.* **2015**, *5*, 85039–85045. [[CrossRef](#)]
64. Horcas, I.; Fernández, R.; Gómez-Rodríguez, J.M.; Colchero, J.; Gómez-Herrero, J.; Baro, A.M. WSXM: A Software for Scanning Probe Microscopy and a Tool for Nanotechnology. *Rev. Sci. Instrum.* **2007**, *78*, 013705. [[CrossRef](#)] [[PubMed](#)]
65. Svenson, S. Controlling Surfactant Self-Assembly. *Curr. Opin. Colloid. Interface Sci.* **2004**, *9*, 201–212. [[CrossRef](#)]

66. Kuong, C.-L.; Chen, W.-Y.; Chen, Y.-C. Semi-Quantitative Determination of Cationic Surfactants in Aqueous Solutions Using Gold Nanoparticles as Reporter Probes. *Anal. Bioanal. Chem.* **2007**, *387*, 2091–2099. [[CrossRef](#)] [[PubMed](#)]
67. Kazakova, J.; García-Povea, A.; Fernández-Palacios, M.; Villar-Navarro, M.; Carnerero, J.M.; Jimenez-Ruiz, A.; Prado-Gotor, R. A Colorimetric Study of the Interaction of Cationic and Anionic Surfactants with Anionic Gold Nanoparticles. *Colloid. Polym. Sci.* **2017**, *295*, 2141–2149. [[CrossRef](#)]
68. Bruce, C.D.; Berkowitz, M.L.; Perera, L.; Forbes, M.D.E. Molecular Dynamics Simulation of Sodium Dodecyl Sulfate Micelle in Water: Micellar Structural Characteristics and Counterion Distribution. *J. Phys. Chem. B* **2002**, *106*, 3788–3793. [[CrossRef](#)]
69. Molero, M.; Andreu, R.; González, D.; Calvente, J.J.; López-Pérez, G. Isotropic Model for Micellar Systems: Application to Sodium Dodecyl Sulfate Solutions. *Langmuir* **2001**, *17*, 314–322. [[CrossRef](#)]
70. Khan, A.M.; Shah, S.S. Determination of Critical Micelle Concentration (Cmc) of Sodium Dodecyl Sulfate (SDS) and the Effect of Low Concentration of Pyrene on Its Cmc Using ORIGIN Software. *J. Chem. Soc. Pak.* **2008**, *30*, 186–191.
71. Williams, R.J.; Phillips, J.N.; Mysels, K.J. The Critical Micelle Concentration of Sodium Lauryl Sulphate at 25 ° C. *Trans. Faraday Soc.* **1955**, *51*, 728–737. [[CrossRef](#)]
72. Freitas, C.; Müller, R.H. Effect of Light and Temperature on Zeta Potential and Physical Stability in Solid Lipid Nanoparticle (SLN[®]) Dispersions. *Int. J. Pharm.* **1998**, *168*, 221–229. [[CrossRef](#)]
73. Mukherjee, A.; Chaudhuri, T.; Moulik, S.P.; Banerjee, M. Internal Charge Transfer Based Ratiometric Interaction of Anionic Surfactant with Calf Thymus DNA Bound Cationic Surfactant: Study I. *Spectrochim. Acta A Mol. Biomol. Spectrosc.* **2016**, *152*, 1–7. [[CrossRef](#)]
74. Imoto, T.; Sumi, S.-I.; Tsuru, M.; Yagishita, K. An Analysis of the Interaction of Sodium Dodecyl Sulfate with Lysozyme. *Agric. Biol. Chem.* **1979**, *43*, 1809–1815. [[CrossRef](#)]
75. Jafari, M.; Mehrnejad, F. Molecular Insight into Human Lysozyme and Its Ability to Form Amyloid Fibrils in High Concentrations of Sodium Dodecyl Sulfate: A View from Molecular Dynamics Simulations. *PLoS ONE* **2016**, *11*, e0165213. [[CrossRef](#)]
76. Biasutti, M.A.; Soltermann, A.T.; García, N.A. Photodynamic Effect in Lysozyme: A Kinetic Study in Different Micellar Media. *J. Pept. Res.* **2000**, *55*, 41–50. [[CrossRef](#)] [[PubMed](#)]
77. Lad, M.D.; Ledger, V.M.; Briggs, B.; Green, R.J.; Frazier, R.A. Analysis of the SDS-Lysozyme Binding Isotherm. *Langmuir* **2003**, *19*, 5098–5103. [[CrossRef](#)]
78. Grueso, E.; López-Pérez, G.; Castellano, M.; Prado-Gotor, R. Thermodynamic and Structural Study of Phenanthroline Derivative Ruthenium Complex/DNA Interactions: Probing Partial Intercalation and Binding Properties. *J. Inorg. Biochem.* **2012**, *106*, 1–9. [[CrossRef](#)] [[PubMed](#)]
79. Bustamante, C.; Vesenka, A.; Lin, C.T.; Rees, W.; Guthold, M.; Keller, R. Circular DNA Molecules Imaged in Air by Scanning Force Microscopy. *Biochemistry* **1992**, *31*, 22–26. [[CrossRef](#)] [[PubMed](#)]
80. International Conference on Harmonization (ICH) Validation of Analytical Procedures: Text and Methodology Q2(R1). 2005. Available online: <https://www.ich.org/page/quality-guidelines> (accessed on 22 January 2023).

Disclaimer/Publisher's Note: The statements, opinions and data contained in all publications are solely those of the individual author(s) and contributor(s) and not of MDPI and/or the editor(s). MDPI and/or the editor(s) disclaim responsibility for any injury to people or property resulting from any ideas, methods, instructions or products referred to in the content.